

AD-A266 139



2

WL-TR-92-3121

**TURBULENCE MODELING FOR
THRUST REVERSER FLOW FIELD
PREDICTION METHODS**



ROBERT E. CHILDS, LAURA C. RODMAN
NIELSEN ENGINEERING & RESEARCH, INC.
510 CLYDE AVENUE
MOUNTAIN VIEW CA 94043-2287

PETER BRADSHAW
STANFORD UNIVERSITY
STANFORD CA 94305

December 1992

Final Report for Period 30 Apr 90 - 31 Dec 92



Approved for public release; distribution is unlimited.

FLIGHT DYNAMICS DIRECTORATE
WRIGHT LABORATORY
AIR FORCE MATERIEL COMMAND
WRIGHT-PATTERSON AIR FORCE BASE, OHIO 45433-6553

93-14000



7028

93 6 22 030

NOTICE

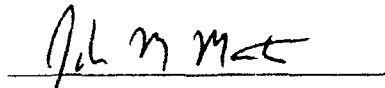
When Government drawings, specifications, or other data are used for any purpose other than in connection with a definitely Government-related procurement, the United States Government incurs no responsibility or any obligation whatsoever. The fact that the government may have formulated or in any way supplied the said drawings, specifications, or other data, is not to be regarded by implication, or otherwise in any manner construed, as licensing the holder, or any other person or corporation; or as conveying any rights or permission to manufacture, use, or sell any patented invention that may in any way be related thereto.

This report is releasable to the National Technical Information Service (NTIS). At NTIS, it will be available to the general public, including foreign nations.

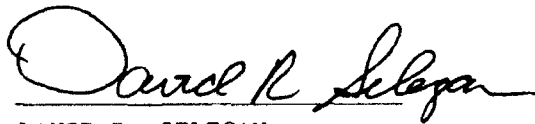
This technical report has been reviewed and is approved for publication.



KENNETH E. WURTZLER
Aerospace Engineer
Applied CFD Section



JOSEPH M. MANTEL
Chief
CFD Research Branch



DAVID R. SELEGAN
Chief
Aeromechanics Division

If your address has changed, if you wish to be removed from our mailing list, or if the addressee is no longer employed by your organization, please notify WL/FIMC, WPAFB, OH 45433-6553 to help us maintain a current mailing list.

Copies of this report should not be returned unless return is required by security considerations, contractual obligations, or notice on a specific document.

REPORT DOCUMENTATION PAGE			Form Approved OMB No. 0704-0188	
<small>Public reporting burden for this collection of information is estimated to average 1 hour per response, including the time for reviewing the instructions, searching existing data sources, gathering the data needed, and reviewing the collection of information, and reviewing the collection of information, and reviewing the collection of information, and reviewing the collection of information. Send comments regarding this burden estimate or any other aspect of this collection of information, including suggestions for reducing the burden, to Washington Headquarters Service, Directorate for Information Operations and Reports, 1215 Jefferson Davis Highway, Suite 1204, Arlington, VA 22202-4302, and to the Office of Management and Budget, Paperwork Reduction Project (0704-0188), Washington, DC 20503.</small>				
1. AGENCY USE ONLY (Leave blank)	2. REPORT DATE	3. REPORT TYPE AND DATES COVERED		
	31 Dec 92	Final 30 Apr 90 to 31 Dec 92		
4. TITLE AND SUBTITLE			5. FUNDING NUMBERS	
Turbulence Modeling for Thrust Reverser Flow Field Prediction Methods			PE - 65502F C - F33615-90-C-3002 PR - 3005 TA - 40 WU - 70	
6. AUTHOR(S)				
Robert E. Childs, Laura C. Rodman, Peter Bradshaw				
7. PERFORMING ORGANIZATION NAME(S) AND ADDRESS(ES)			8. PERFORMING ORGANIZATION REPORT NUMBER	
Nielsen Engineering and Research, Inc. 510 Clyde Ave Mountain View CA 94043			NEAR TR 457	
9. SPONSORING / MONITORING AGENCY NAME(S) AND ADDRESS(ES)			10. SPONSORING / MONITORING AGENCY REPORT NUMBER	
Ken Wurtzler (513) 255-3761 WL/FIMC 2645 Fifth St Ste 7 Wright-Patterson AFB OH 45433-7913			WL-TR-92-3121	
11. SUPPLEMENTARY NOTES				
12a. DISTRIBUTION / AVAILABILITY STATEMENT			12b. DISTRIBUTION CODE	
Approved for public release; Distribution is unlimited.				
13. ABSTRACT (Maximum 200 words)				
<p>The use of thrust reversing on aircraft operating in ground effect produces complex flow fields, for which conventional turbulence models are inadequate. The main objective of the work was to produce an improved turbulence model. The work included experimental measurements of an impinging jet inclined 45 degrees into the crossflow. Large eddy simulation (LES) was used to identify the dominant turbulent physics in these flows and to guide the development of an improved k-ε model for Reynolds-averaged calculations. Modifications to the k-ε model for the effects of streamline curvature and vortex stretching (lateral divergence) were used. Compared to the original k-ε model, the modified model reduced by as much as 70 percent the errors in predicting the ground vortex location.</p>				
14. SUBJECT TERMS			15. NUMBER OF PAGES	
Impinging Jets, Turbulence Modeling, Computational Fluid Dynamics			69	
			16. PRICE CODE	
17. SECURITY CLASSIFICATION OF REPORT	18. SECURITY CLASSIFICATION OF THIS PAGE	19. SECURITY CLASSIFICATION OF ABSTRACT	20. LIMITATION OF ABSTRACT	
Unclassified	Unclassified	Unclassified	UL	

CONTENTS

Section	Page
LIST OF FIGURES.....	ii
SYMBOLS AND ABBREVIATIONS	iv
EXECUTIVE SUMMARY	vi
1. INTRODUCTION	1
Objectives	4
2. EXPERIMENTAL STUDY	6
3. NUMERICAL METHODS	15
Navier-Stokes Equations	15
Spatial Discretization Scheme	16
High-Accuracy Spatial Interpolation	16
Spatial Accuracy in Fourier Space	18
Viscous Fluxes	19
Boundary Conditions	20
Time Integration	22
4. LARGE EDDY SIMULATIONS	24
Dynamical LES Results for Normal Impingement	25
Dynamical LES Results for the Primary Test Case	29
Statistical Results for Normal Impingement	33
5. TURBULENCE MODELING	39
Modifications to the $k-\epsilon$ Model	40
Streamline Curvature	40
Vortex Stretching	41
Model Calibration	44
6. REYNOLDS-AVERAGED IMPINGING JET CALCULATIONS	46
Case I: Normal Jet, $H/D = 3$, $V_j/V_\infty = 5$	46
Case II: Normal Jet, $H/D = 3$, $V_j/V_\infty = 10$	52
Case III: Inclined Impinging Jet	53
Interpretation of Reynolds-Averaged Results	56
7. CONCLUSION	58
Recommended Future Work	58
REFERENCES	60

FIGURES

		Page
Figure 1.	Sketch of jet with thrust reversers in ground effect.....	1
Figure 2.	Diagram of wind tunnel.....	6
Figure 3.	Velocity uniformity at inlet to wind tunnel test section from total pressure survey.....	8
Figure 4.	Boundary layer profile at inlet to wind tunnel test section.....	9
Figure 5.	(a) Nozzle exit velocity profile.....	9
	(b) Near-wall velocity profile	10
Figure 6.	Smoke visualization photograph of inclined impinging jet.....	10
Figure 7.	Deflection angles at jet exit.....	11
Figure 8.	Surface static pressure distributions for primary test case.....	12
Figure 9.	Surface static pressure distributions for several velocity ratios.....	13
Figure 10.	Surface centerline skin friction.....	14
Figure 11.	Accuracy of spatial discretization, defined in Eq. 16.	19
Figure 12.	Contours of Mach number and vorticity magnitude for normal impinging jet.	
	(a) Mach number.....	26
	(b) Vorticity magnitude.....	26
Figure 13.	Time sequence of vorticity contours for normal impinging jet.....	27
Figure 14.	Contour plots of instantaneous vorticity, turbulence energy $(u'u' + v'v' + w'w')/2$ and the shear stress, $u'v'$.	
	(a) Vorticity.....	28
	(b) Turbulence energy.....	28
	(c) Shear stress.....	29
Figure 15.	Instantaneous Mach number contours on a plane normal to the jet and above the impingement zone, for the normal impinging jet.....	30
Figure 16.	Top view of instantaneous Mach number contours and velocity vectors at $y = 0.3$, for normal impinging jet case.	
	(a) Mach number.....	30
	(b) Velocity vectors.....	32
Figure 17.	Contours of Mach number and vorticity magnitude on the center plane, for inclined jet case, and vorticity contours at a later time showing vortex evolution.	
	(a) Mach number.....	31
	(b) Vorticity magnitude, time = 55.....	32
	(c) Vorticity magnitude, time = 64.....	32
Figure 18.	Velocity vectors at $y = 0.03$ (at every other grid point) showing lateral divergence, $-\partial w / \partial z$, in regions of vortex intensification.....	33
Figure 19.	Mean Mach number and pressure contours, and velocity vectors on center plane of normal impinging jet, computed from time average of LES results.	
	(a) Mach number.....	34
	(b) Pressure contours.....	35
	(c) Velocity vectors.....	35
Figure 20.	Contour plots of turbulent statistics on center plane of normal impinging jet, computed from time average of LES results.	

	(a) Turbulent kinetic energy.....	36
	(b) Normal stress, $u' u'$	36
	(c) Normal stress, $v' v'$	37
	(d) Shear stress, $u' v'$	37
Figure 21.	Growth rates of self-preserving wall jet on a logarithmic spiral, experiment and calculations with the STD and C models.....	45
Figure 22.	Velocity magnitude contours and velocity vectors on the center plane, computed with the CVS model, for Case I.	
	(a) Velocity magnitude.....	46
	(b) Velocity vectors.....	47
Figure 23.	Surface centerline static pressure distribution for Case I.....	48
Figure 24.	Comparison of center plane mean velocity vectors for Case I computed with the CVS model and measured by Cimbala et al. ²⁹	
	(a) Measured velocity.....	48
	(b) Measured velocities.....	49
Figure 25.	Comparison of $u' v'$ on the center plane of Case I computed with the STD and CVS models.	
	(a) STD model.....	50
	(b) CVS model.....	50
Figure 26.	Surface centerline pressure distributions computed in grid refinement study.	
Figure 27.	Comparison of center plane mean velocity vectors for Case II computed with the CVS model and measured by Cimbala et al. ²⁹	
	(a) Measured velocities.....	52
	(b) Predicted velocities.....	53
Figure 28.	Contours of velocity magnitude, velocity vectors, and contours of the shear stress $u' v'$ on the center plane for Case III predicted with the CVS model.	
	(a) Velocity magnitude.....	54
	(b) Velocity vectors.....	55
	(c) Shear stress.....	56
Figure 29.	Surface centerline static pressures for Case III.....	56

DTIC QUALITY INSPECTED 2

Accession For	
NTIS CRA&I	<input checked="" type="checkbox"/>
DTIC TAB	<input type="checkbox"/>
Unannounced	<input type="checkbox"/>
Justification	
By	
Distribution /	
Availability Codes	
Dist	Avail and/or Special
A-1	

SYMBOLS AND ABBREVIATIONS

D	Diameter
$D() / Dt$	Substantial derivative, $= \partial() / \partial t + U_i \partial() / \partial x_i$
C	Model coefficients
e	Total specific internal energy, Eq. (5)
F	Flux of Q, Eqs. (3-16)
k	Turbulence kinetic energy
H	Height above ground of jet nozzle
L	Turbulent mixing length
M	Mach number
n	Normal to streamline along radius vector
P	Production term
p	Pressure
Pr	Prandtl number
Q	Flow variables
R	Radius of jet or streamline curvature
Re	Reynolds number
s	In the streamwise direction
S	Source terms
S_{ij}	Strain rate tensor, Eq. (43)
t	Time
u, v, w	Instantaneous velocities
U, V, W	Average velocities
V	Velocity magnitude, occasionally
u', v', w'	Fluctuating velocities
x, y, z	Spatial coordinates
$y_{1/2}$	y at which $U / U_{\max} = 1/2$
β	Streamline curvature stability parameter
δ	Boundary layer thickness
δ	Discrete approximation of ∂
$\Delta x, \Delta y, \Delta z$	Grid spacing
χ	Vortex stretching magnitude, Eq. (41)
ε	Rate of dissipation of k
ε_{ijk}	Alternating third rank tensor
ϕ	Angle of jet
θ	Velocity direction
λ	Wave length
μ	Viscosity
σ	Model coefficient
ρ	Density
τ	Viscous and/or turbulent stress
ω	Wave number
Ω_j	Mean vorticity tensor

Superscripts and Subscripts

$\overline{()}$	Temporal or spatial average
u_i	Cartesian tensor indices
$()_j$	Of the jet
$()_j$	Denoting a grid point, Eqs. (8-20)
$()_k$	Of the turbulence kinetic energy
$()_t$	Of the turbulence
$()_\infty$	Of the freestream

Model Designations

STD	Standard model defined by Eqs. (24-29),
C	With curvature modification, Eqs. (38, 39),
VS	With vortex stretching modification, Eqs. (40-44),
CVS	With curvature and vortex stretching modifications.

EXECUTIVE SUMMARY

Thrust vectoring is one means of improving the maneuverability and take-off and landing performance of aircraft. However, thrust vectoring, especially in close proximity to the ground, can increase significantly the complexity of the flow field around the aircraft, and make aircraft design more difficult. To achieve good aircraft designs in spite of the complex flow, it is necessary to have an accurate flow prediction method. Methods based on the Reynolds-averaged Navier-Stokes equations can make these predictions, if the numerical discretization and the turbulence modeling are sufficiently accurate. This work addresses the issue of turbulence modeling for the inclined impinging jets associated with the use of thrust reversing in ground effect.

Large eddy simulations (LES) and physical experiments were conducted to obtain mean flow and turbulence data. These data were analyzed to identify the dominant physical processes which govern turbulence in these flows. Streamline curvature and vortex stretching were identified as the two most significant influences on turbulence in these flows which are not treated adequately in the standard $k-\epsilon$ model. Modifications which account for curvature and vortex stretching were added to the standard $k-\epsilon$ model. The new coefficients in the resulting modified turbulence model were determined via numerical optimization for benchmark jet flows unrelated to the impinging jet flows of primary concern.

In three cases considered, two impinging jets issuing from a nozzle normal to the ground plane and one issuing from a nozzle inclined 45° into the crossflow, the modified model consistently improved the accuracy for the computed location of the ground vortex. Errors in the computed vortex location, relative to the distance between the impingement point and the ground vortex core, were as large as 50% in calculations with the standard $k-\epsilon$ model and could be of either sign (overprediction or underprediction of the ground vortex's forward extent). The modified model reduced these errors to the range of 13%-18%, and it consistently overpredicted the upstream penetration of the ground vortex.

1. INTRODUCTION

Because of recently defined tactical threats it is desirable to improve the maneuverability and take-off and landing performance of aircraft. The use of exhaust jet thrust vectoring, including thrust reversing, is one means of achieving these improvements. However, thrust vectoring can increase significantly the complexity of the flow field around the aircraft, and make aircraft design more difficult. To achieve good aircraft designs in spite of this difficulty, it is necessary to have an accurate flow prediction method. The flight regime which is perhaps the most difficult to predict accurately is that of an aircraft landing with thrust reversers operating. The flow from the reversed jets creates a complex flow environment which includes an upwash and ground vortex, for example, as sketched in Figure 1.

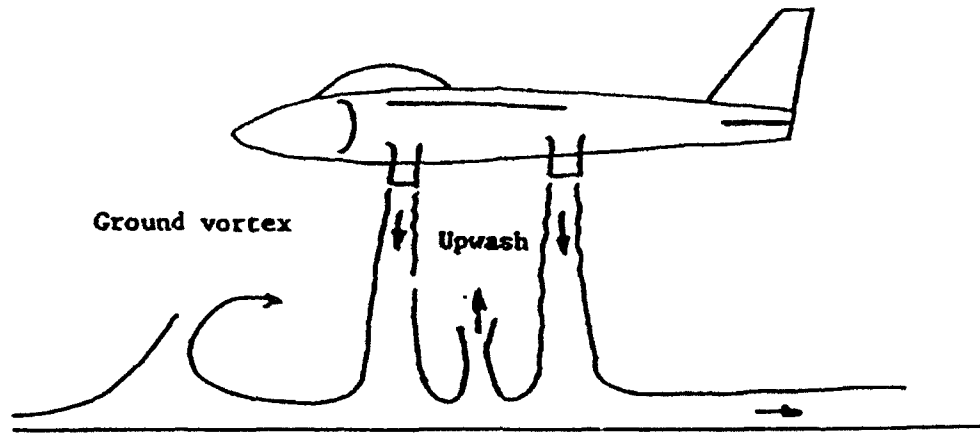


Figure 1. Sketch of jet with thrust reversers in ground effect.

The effects of operating thrust reversers in ground effect have been investigated experimentally in, for example, References 1-3. There are at least two primary problems caused by the use of thrust reversers. One is that forces and moments acting on the aircraft are affected significantly by the reverser plume. The other is that hot exhaust gases and debris from the ground may be thrown up near the front of the aircraft and ingested by the engine, which causes power loss and engine damage. Both the ground vortex and upwash can be highly unsteady, although that unsteadiness is usually at a frequency which exceeds the response frequency of the aircraft. There may be other problems associated with thrust reversing, for example, the thermal and acoustic loads which affect the aircraft or undercarriage stores.

The stability and control problems caused by thrust reversing depend strongly on the aircraft's proximity to the ground. Out of ground effect, 20%-45% reductions in the effectiveness of the horizontal tail have been noted, while the effectiveness of the vertical fins and ailerons were essentially unaffected. In ground effect all control surfaces are affected.¹ Changes in aircraft's lift coefficient of the order of +0.15/-0.9 and changes in pitching moment of the order of +0.5/-0.1 have been observed by Blake.³ These forces depend on the forward deflection and outward cant of the reversing jets, the ratio of jet to freestream dynamic pressures, on the height above the ground, and the side slip angle.

The problem of hot gas and debris ingestion has long been a research issue for VTOL aircraft,^{4,6} because engines must be operated near maximum power for the aircraft to hover and, hence, in danger of compressor stall if hot gases are ingested. Both the ground vortex and the upwash fountain may contribute to contaminant ingestion by causing jet exhaust gases to flow up and in front of the aircraft. On an aircraft landing with thrust reversers, the primary factors which determine if contaminant ingestion will occur are the pattern and the forward extent of the ground vortex.

Prediction Methods - The use of an accurate flow prediction method based on the Navier-Stokes equations is a valuable means of understanding the above problems and designing aircraft to avoid them. Navier-Stokes prediction methods are being used in a wide variety of research and design efforts because they are cost-effective, fast to use and can provide flow details which are often not obtained in experimental studies. Many experimental programs now include a complementary computational program as a means of enhancing the value of the experiments. With the development of improved computers and numerical algorithms, the accuracy and capabilities of these prediction methods has increased significantly in the past few years. Further improvements are expected. However, there is one critical area in which improvements are not being made rapidly, and that is turbulence modeling.

The turbulence generated in ground effects flows is far more complex than in aerodynamic flows on conventional aircraft at moderate incidence, and it has a strong effect on the complete flow field. The ground vortex and upwash fountain are strongly dependent on turbulent mixing, and they can exert a strong influence on aerodynamic characteristics in ground effect.

Turbulence Modeling - Many aspects of turbulence in ground effects flows are not predicted well by existing Reynolds-averaged turbulence models. For example, the size and location of the ground vortex is predicted poorly by the Baldwin-Lomax model and by the standard $k-\epsilon$ model. The shear stresses in the upwash fountain are underpredicted by as much as an order of magnitude by the $k-\epsilon$ model, the Algebraic Stress Model (ASM), and the Reynolds-Stress transport model (RSTM).⁷ These flows are highly dependent upon turbulent momentum transport, and the errors in the predicted turbulence create large errors in the mean flow predictions. The magnitude of these modeling errors may render existing flow prediction methods almost useless for studies of the thrust reverser effects on landing aircraft.

The prospects for developing improved turbulence models by conventional means is not good. The turbulence mechanisms which are important in these flows are more complex than in typical aerodynamic flows. They are also more powerful in impinging flows, meaning that they produce larger and more rapid changes in turbulence than in typical aerodynamic flows. A "turbulence mechanism" denotes anything that affects the turbulence in a flow. For example, the conversion of mean flow kinetic energy into turbulence kinetic energy due to the interaction between turbulent stresses and mean flow gradients is one such mechanism. Many of these mechanisms are difficult or impossible to identify in experimental data, and they can have a strong impact on these flows. Because of the rapid spatial variations in the mean flow, turbulence mechanisms can also change

rapidly. Some modeling concepts which are widely employed, such as isotropy and the use of an eddy viscosity, may be invalid for these flows.

The technology of large eddy simulation (LES) provides a means of obtaining the turbulence data which are required to identify and model the critical turbulence mechanisms in these flows. LES involves numerical simulations of fluid flow, based on the unsteady Navier-Stokes equations, which resolve the mean flow and the large scales of turbulence. Hence, LES can represent with good accuracy the dominant features of a turbulent flow. All turbulence information in an LES can be recorded, and virtually any turbulence characteristics can be studied. The detailed knowledge of turbulence provided by LES is essential to identifying and modeling the complex mechanisms which occur in thrust reverser flows.

Previous studies of thrust vectoring in ground effect have focused largely on vertical jets used with Vertical Take-off and Landing (VTOL) aircraft, and the specific problems of thrust reversing have not been addressed on a fundamental basis. Therefore, the specific fluid mechanical problems associated with thrust reversing are not well understood. Given the limited understanding of turbulence in impinging jets, it is reasonable to expect that changing the inclination of the jet roughly 45° may have a significant effect on the turbulence. Hence, measurements of turbulence in thrust reverser-like flows are needed. One study which included inclined jets⁸ involved only flow visualization, which does not provide the information required to develop improved turbulence models.

Modeling Priorities - In a previous study by some of the same authors, various aspects of the types of flows which could be generated in thrust reverser applications were evaluated. The following list assigns priorities to the generic flow phenomena for which improved turbulence models are most critically needed, based on that flow's importance to aircraft safety and performance, and on the shortcomings of existing turbulence models.

1. The ground vortex exerts a strong influence on most aerodynamic characteristics, such as lift, pitching moment, and rolling moment, and it can cause contaminant ingestion. The position of the ground vortex is not predicted well by algebraic models or the standard $k-\epsilon$ model. The ground vortex flow consists of the vortex itself and other closely associated regions, the wall jet and the impingement zone.

The wall jet is one distinct flow region of the ground vortex. The forward extent of the ground vortex is largely determined by the deceleration and separation of the wall jet. The wall jet beneath the ground vortex is significantly different from that in many laboratory experiments in that it has a complex vortical flow above it, and it is highly three-dimensional. The accuracy with which this region of flow can be computed is not known.

The impingement zone is where the jet strikes the ground and spreads out into a wall jet. The jet flow must pass through this region before reaching the upwash and the ground vortex, so that inaccuracy here will propagate to most of the ground effects region. This region is predicted poorly by the standard $k-\epsilon$ model, although it appears that means for significantly improving the accuracy in this region exist.

2. The upwash fountain and related flow phenomena tend to throw contaminants up and in front of an aircraft where they can be ingested. In experiments this problem does not appear to be as serious as the ground vortex. However, various Navier-Stokes calculations, performed at Nielsen Engineering & Research (NEAR), NASA/Ames Research Center, and NASA/Lewis Research Center, all predict the upwash-like phenomena to be more significant than the ground vortex for causing ingestion problems. This result is not supported by experiment. Accurate modeling of the upwash and related phenomena is required to reduce its predicted effect to a realistic magnitude.
3. A free jet in a crossflow is the first phenomenon to occur as the flow emerges from the thrust vectoring apparatus. As the crossflow interacts with the jet, two counter rotating vortices are formed on the sides of the jet. If the jet is adjacent to a vertical stabilizer, the vortices combined with the blockage effect of the jet can significantly alter the pressure acting on the fin. Turbulence in vortices is not modeled well by existing models. The effects of the mean and turbulence quantities at the jet exit can play a significant role in the jet's development.
4. Dynamical effects, due to the rate of descent of the aircraft, are important. It is not currently known if modeling of dynamical effects on turbulence is a research issue. The time scales for turbulence are much shorter than for the mean flow, so that a quasi-steady model may suffice. Also, the accuracy for steady state flows is very poor, at present, and must be improved before an attempt at modeling unsteady flow is appropriate.

The ground vortex and upwash are the most critical to be able to predict accurately. If they can be predicted accurately, it is likely that the other phenomena can be predicted because they are governed by many of the same turbulence mechanisms which occur in the first two.

Objectives

The objectives of this work are to develop and to validate a Reynolds-averaged turbulence model for thrust reverser flow fields. Successful completion of this work will yield an accurate mathematical model of turbulence which can be incorporated into Navier-Stokes prediction codes for application to thrust reverser problems. To achieve these goals, several intermediate objectives must be met.

The first objective is to obtain good turbulence data for these flows so that the mechanisms which control turbulence can be evaluated. Data will be obtained from experiments and from large eddy simulations (LES) of impinging jet flows. Experiments are needed because they provide trustworthy data which is accurate to within some experimental uncertainty. However, some important turbulence data, for example, two-point correlations and fluctuating pressures, are difficult or impossible to obtain from physical experiments, at present. Therefore, LES will also be performed to obtain data which are currently inaccessible in experiments.

The next objective is to identify the mechanisms which control turbulence in the various flow regions. Streamline curvature, anisotropy, and large scale mixing are

important mechanisms in the upwash, and they are expected to be important in other regions, as well. These are fundamental mechanisms which are somewhat understood, and which can be identified in the LES results. There are also other mechanisms which are not yet well understood. For example, the position of the ground vortex is determined by the deceleration and separation of a wall jet beneath a vortical outer flow moving in the opposite direction. The mechanisms which control this process have not yet been identified, but they must be understood if a model which can accurately predict the forward penetration of the ground vortex is to be developed.

The third objective is to develop modifications to the $k-\epsilon$ model which account for the dominant additional turbulence mechanisms associated with jet impingement. Based on the understanding of turbulence mechanisms, a model or models will be developed which mimic the turbulence behavior observed in the experiments and LES. Model development is one of the most critical steps in the proposed work. Many individual mechanisms are poorly understood at present and predicted poorly or not at all by most turbulence models. The model must also be optimized to give the best possible accuracy for the range of flow phenomena which occurs in thrust reverser flow fields. This will involve "fine tuning" the model to give good agreement with LES and experimental data.

The final objective is to validate the accuracy of the model which is developed. The turbulence model will have been developed and optimized for the specific phenomena which occur in a few critical regions of thrust reverser flows. It is important to determine how well the model performs for complete experimental flow fields. If the model does have significant shortcomings for the complete flow field, it will be necessary to tune the model further to give the best possible overall accuracy. If significant errors still persist, it is essential to know where they occur and how large they are.

2. EXPERIMENTAL STUDY

This part of the project was performed in the Mechanical Engineering Department of Stanford University by Prof. P. Bradshaw and several research assistants.

Although the target flow is a hot, transonic jet moving relative to the ground, the main problems in turbulence modeling will occur in a low-speed, isothermal flow in which the jet is stationary relative to the ground. The results will be quantitatively different from the hot, high-speed flows resulting from engine exhaust jets. However, data from the low-speed case can provide a good understanding of the qualitative characteristics of thrust reverser flows.

Wind Tunnel - The tunnel used for this experiment is an open-circuit, suck-down tunnel designed especially for smoke-flow visualization. The intake consists of a 30 in x 30 in bell-mouth followed directly by a flow-management section. In this section, the incoming flow passes through a 1 in long honeycomb straightener of 0.5 in cell diameter and then through a set of four screens. The screens are separated by 1.5 in and each has a pitch of 38 wires/inch. The wire diameter is 0.006 in which translates to an open area ratio of 0.596. There is no contraction to the working section which begins immediately downstream of the screens. A diagram of the tunnel is given in Figure 2.

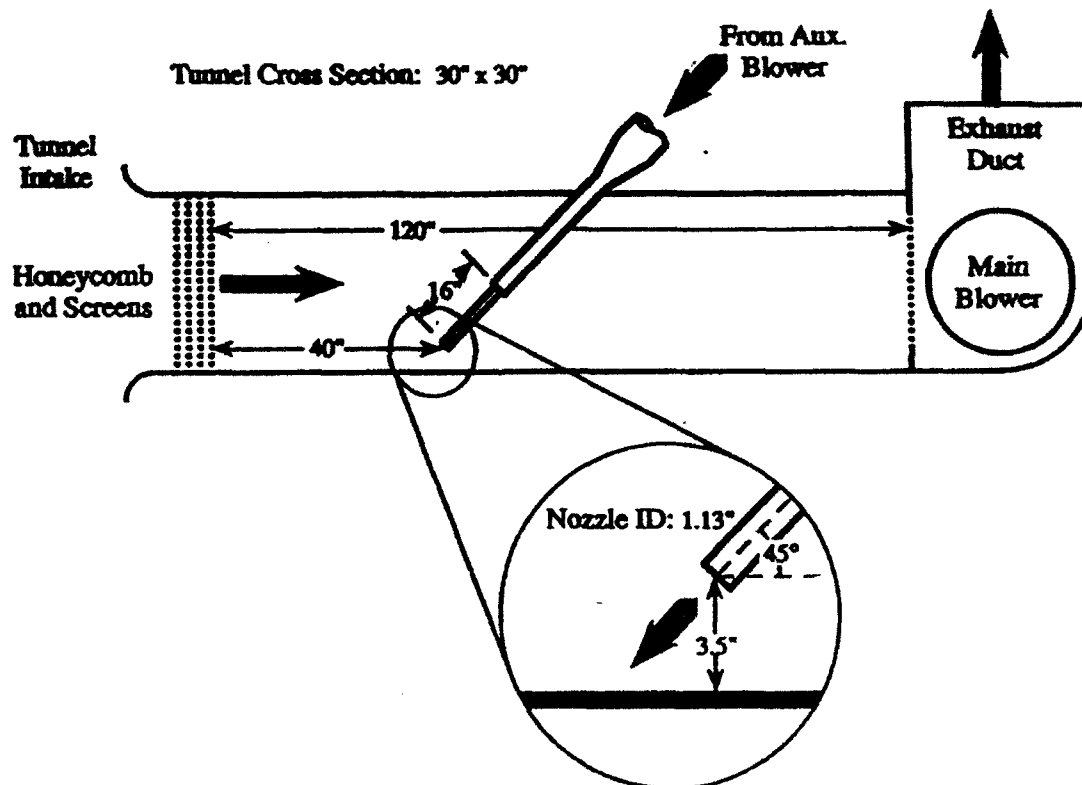


Figure 2. Diagram of wind tunnel.

The working section floor is made from particle board which has been painted black to reduce glare during flow visualization. The walls are made from 1/4 in Plexiglass, and the

roof is formed by interchangeable particle-board panels. Although constant cross section is maintained for a length of 120 in, the end of the working section is effectively defined by the region where interference from the exit begins (roughly 90 in from the start of the test section).

The pressure drop through the tunnel is supplied by a 20.8 in intake-diameter, centrifugal blower driven by a constant speed motor. For this experiment, the maximum flow rate of 16 ft/s is desired. The flow rate is measured by a pitot-static port downstream of the flow-management section.

Cross-flow Jet - An auxiliary blower is used to power the cross-flow jet. The intake to this blower is restricted by a perforated aluminum sheet and a butterfly valve which can be adjusted to maintain a constant ratio of bulk-average jet speed to tunnel speed of 4.36. The outflow is led through a 4.25 in diameter flexible duct to a contraction which leads into a 2 in inside diameter feed pipe. At the entrance to this pipe is a 2.5 in section of aluminum honeycomb with a 1/4 in cell diameter. The feed pipe passes through the roof at 45° and extends 23 in into the tunnel. The end of this pipe is supported by an aluminum "sting" which is supported by aluminum rods fastened to the floor. A conical contraction takes the flow into the 1.131 in inside diameter nozzle section.

The nozzle section extends for 16 in ending with its exit plane inclined at 45° and its center 3.5 in above the working section floor and 39 in downstream of the final screen. (See Figure 2.) While a contraction at the nozzle exit could have provided uniform flow, it was felt more important to minimize the nozzle area and thus its interference with the flow. Furthermore, the flow exiting actual thrust reversers will probably be highly turbulent because of the engine turbulence and the turning vanes. Thus, the reversed engine exhaust is more closely approximated by a turbulent pipe flow than a jet from a large area-ratio contraction. The flow rate is measured by a pitot tube in the contraction to the feed pipe and a static port 3 in from the exit of the nozzle. A Plexiglass template was manufactured to check the alignment of the jet nozzle.

Tunnel Calibration - A series of tests were run to determine the quality of the flow entering the working section of the tunnel. The first test was a total pressure survey 3 in downstream of the flow-management section. An initial traverse indicated significant non-uniformity in the velocity field. The results of a second survey, performed after cleaning the screens, are shown in Figure 3, and represent a marked improvement. In order to keep dirt and dust interference from altering the flow field, the screens must be cleaned after every 2 hours of tunnel operation.

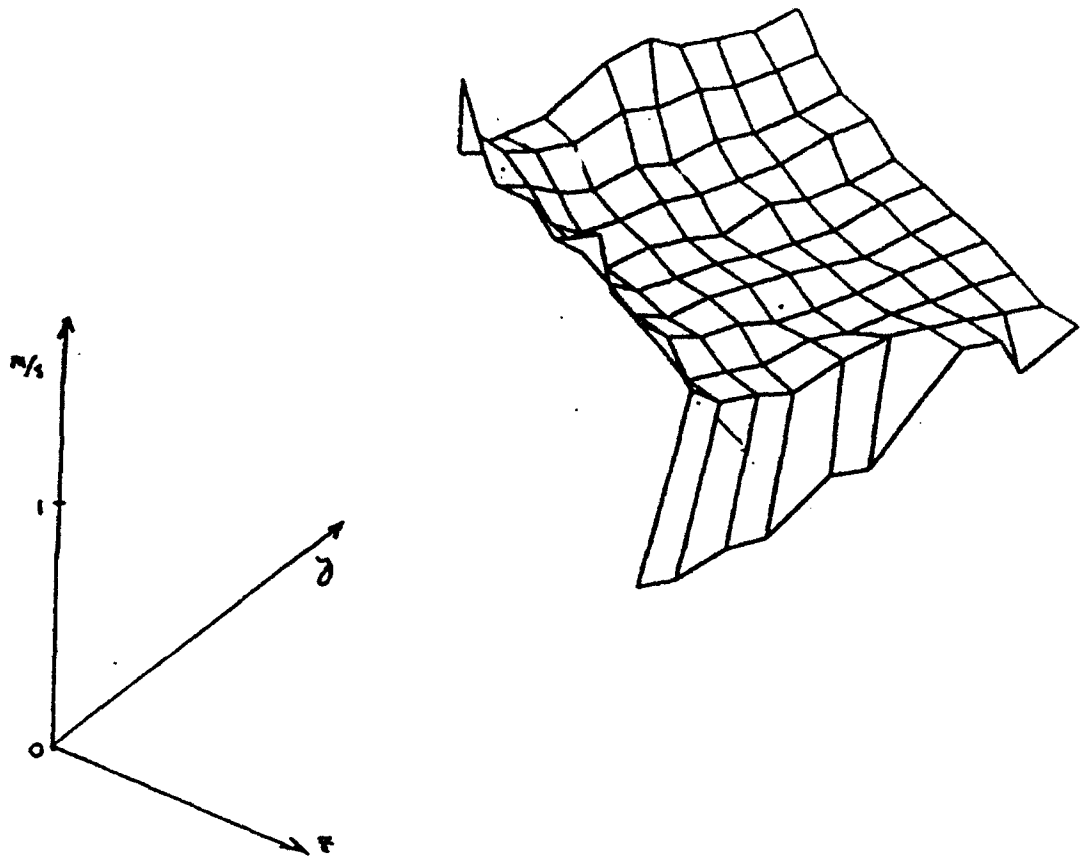


Figure 3. Velocity uniformity at inlet to wind tunnel test section from total pressure survey.

The second diagnostic test was a series of total pressure traverses of the floor boundary layer. These were done on the tunnel center-plane at distances of 7 and 16 inches from the final screen, with a 1/8 in high trip of square cross section placed 3 in downstream of the screens. The first profiles revealed a surprisingly large boundary layer thickness. An investigation was done to determine if this was a result of dirty screens, intake geometry, or trip shape. Comparing a traverse done without the trip to one made of the roof boundary layer suggested the trip was the culprit. Replacing the square trip with a cylinder of equal height, faired by a tape strip, resulted in the boundary layer shown in Figure 4. This layer is felt to be of acceptable thickness. The "wiggles" near the top of the layer do not appear in traverses done without the trip and are felt to be a consequence of the trip.

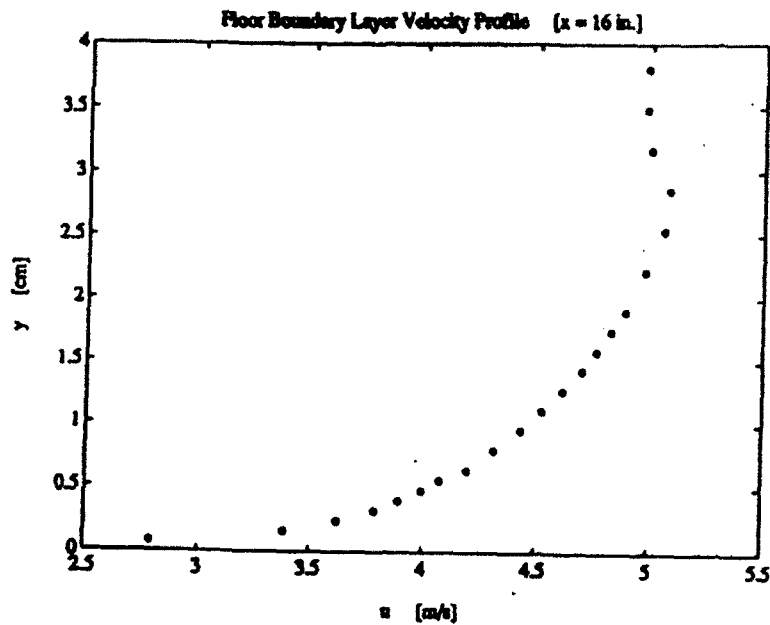
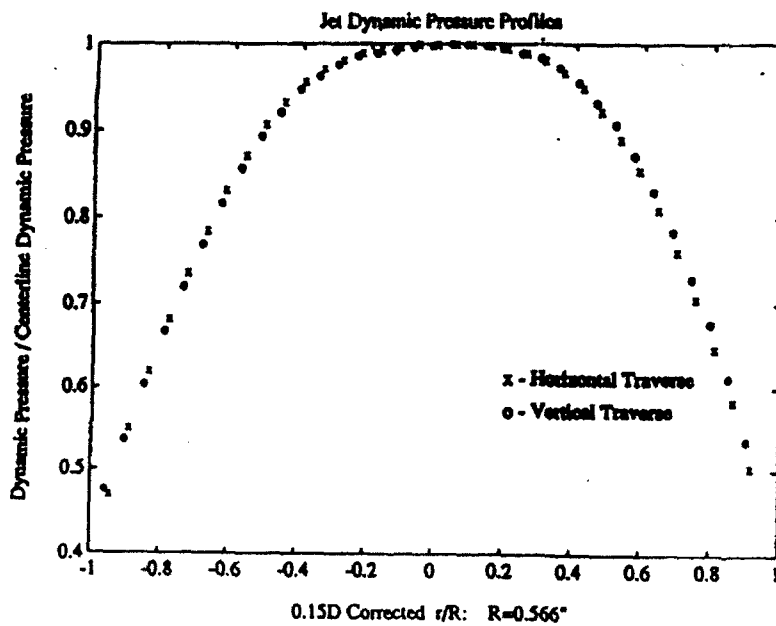
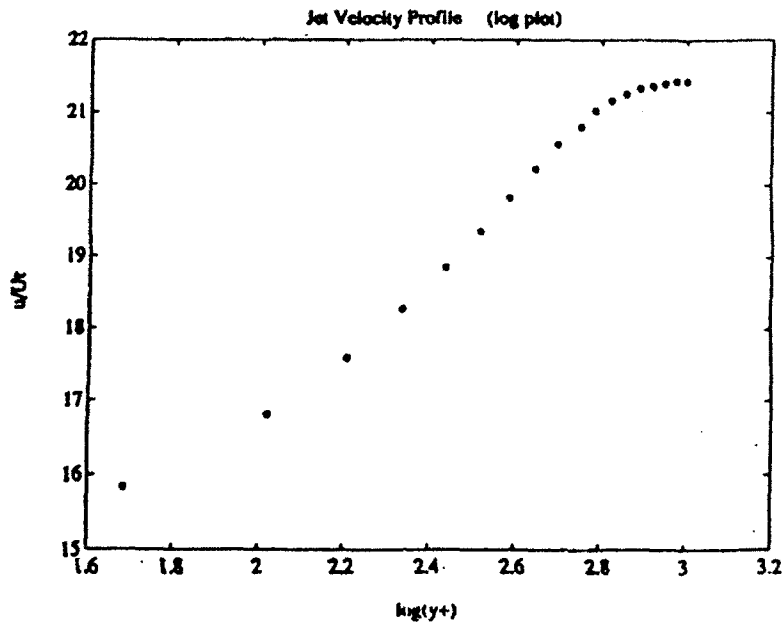


Figure 4. Boundary layer profile at inlet to wind tunnel test section

Jet Calibration - Vertical and horizontal traverses of the jet were performed at a station 0.55 in inside the nozzle. The results of these traverses are shown in Figure 5-a along with computed mass and momentum flow rates. In order to compare with the "law of the wall" profile, shear stress measurements were made at the nozzle wall and a logarithmic plot of u^+ vs. y^+ was generated. This plot, along with the law of the wall profile, is shown in Figure 5-b.



(a) Nozzle exit velocity profile



(b) Near-wall velocity profile

Figure 5.

Selection of the Primary Test Case - In order to generate a flow field representative of a thrust reverser, a series of flow visualization experiments were done to select the angle of the nozzle and its height above the floor. With the flow into the auxiliary blower fully restricted, the nozzle rotated to $\phi = 43.3^\circ$ forward of vertical and the center of the nozzle 3.57 in above the floor, the flow pattern shown in Figure 6 resulted. The final geometry was fixed very near this setting because it was decided that this configuration provided a representative recirculation of the reversed flow. The actual geometry shown in Figure 2 was selected because it provides round figures for the test case.

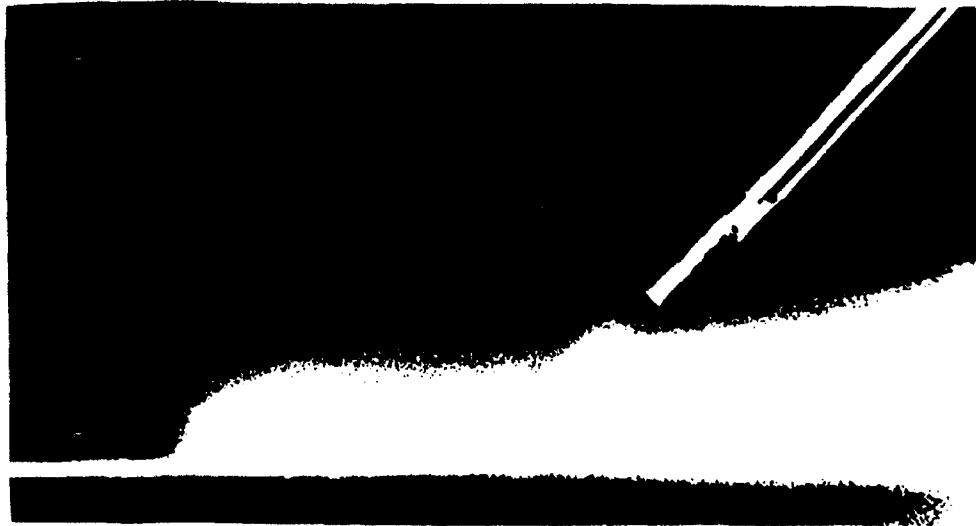


Figure 6. Smoke visualization photograph of inclined impinging jet.

The primary inclined jet test used in this experiment and computed in Reynolds-averaged and large eddy simulation, described later, is defined by the following operating conditions:

$\phi = 45^\circ$	nozzle angle forward of straight down
$U_\infty = 16 \text{ ft./sec}$	crossflow velocity
$H_j/D_j = 3.09$	nozzle height to diameter ratio
$V_{j,\text{max}}/V_{j,\text{bulk}} = 1.208$	maximum to bulk jet velocity ratio
$V_{j,\text{max}}/U_\infty = 5.266$	jet maximum to crossflow ratio

Boundary Conditions - In order to model the flow computationally, appropriate boundaries must be selected and the flow field determined there. For this flow, the in-flow boundaries are a tunnel cross section downstream of the trip and the nozzle exit plane. These measurements should be performed with both the tunnel and the jet running. However, the tunnel inflow conditions were measured with the jet turned off. These include the boundary layer traverses already mentioned. The jet exit conditions were measured with a three tube yawmeter with the tunnel running. The purpose of the jet traverse was to determine how much the free-stream deflects the jet exit flow. The results of this traverse are shown in Figure 7.

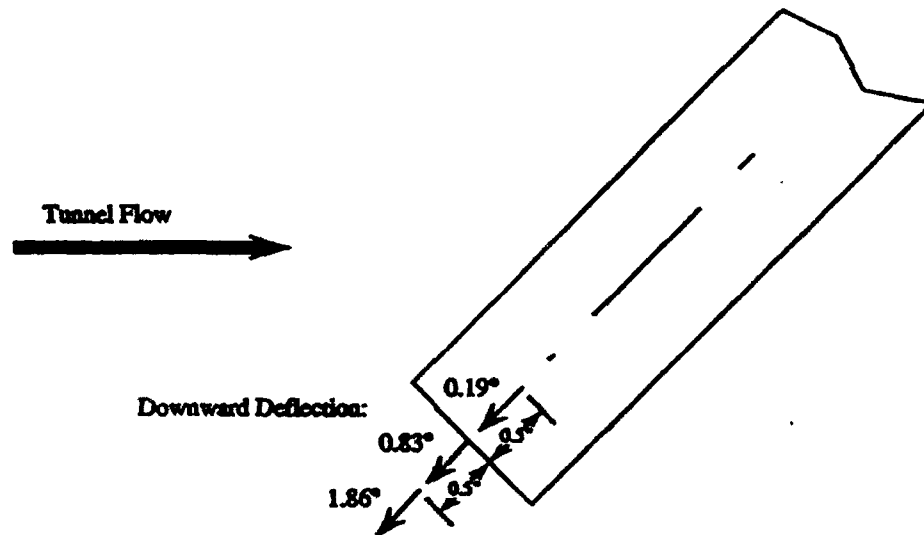


Figure 7. Deflection angles at jet exit.

Floor Static Pressure Distribution - The static pressure distribution along the centerline of the floor was measured by means of an array of pressure taps built into the floor. The spacing of these taps was chosen to provide a high density of measurements in the

regions of rapidly changing pressure. The results of the static pressure traverse for the primary test case are shown in Figure 8.

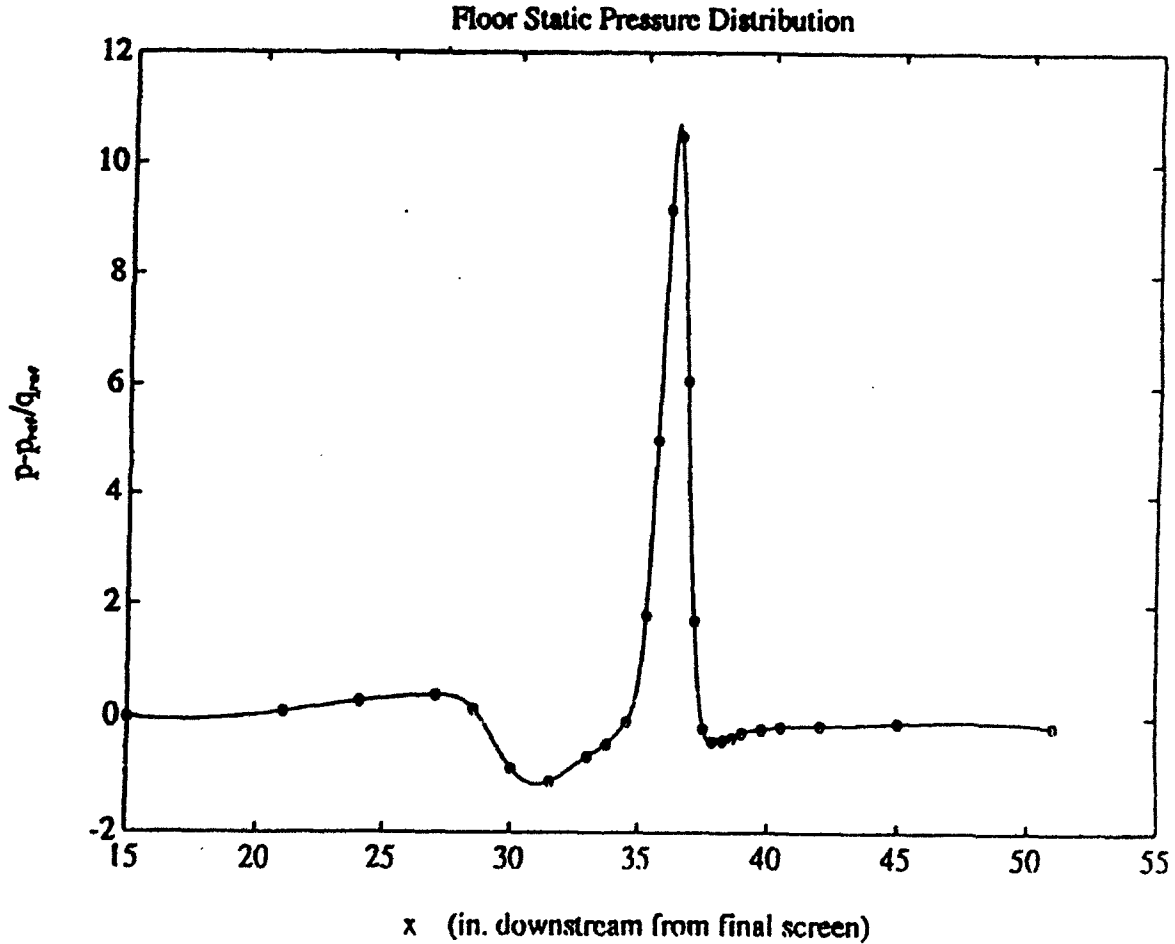


Figure 8. Surface static pressure distributions for primary test case.

To provide data for model testing, the jet velocity was varied over a wide range while the jet height and angle were held constant. The surface static pressures are given in Figure 9 for several jet velocities. The ground vortex does move forward with increasing jet velocity, and there are changes in the shape of the pressure distribution as the velocity ratio changes. Note that the scale of these figures changes to accommodate the changing velocity ratio.

Cp along centerline

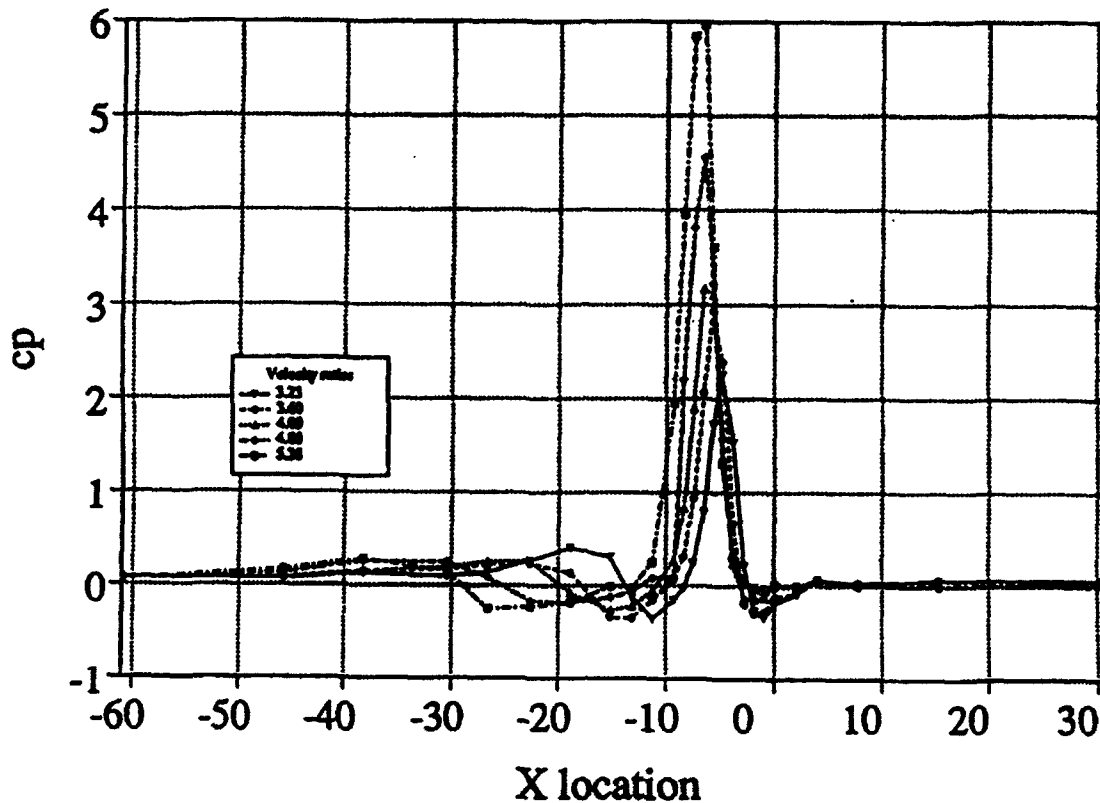


Figure 9. Surface static pressure distributions for several velocity ratios.

Floor Shear Stress Distribution - The shear stress distribution was measured in the same region as the static pressure distribution by means of a Preston tube traverse. The outside diameter of the Preston tube used was 0.127 in and the calibration used was that of Patel.⁹ In order to make shear stress measurements in the reversed flow regions, a complete traverse was made with the probe facing the tunnel entrance, followed by a similar traverse with the probe direction reversed. The pressure difference at any given location was taken to be the greater of the two measurements. The shear stress distribution appears in Figure 10. Note, however, that this data corresponds to a flow configuration of $\phi = 43.3^\circ$ and $H/D = 3.16$, which is slightly different from the primary test case.

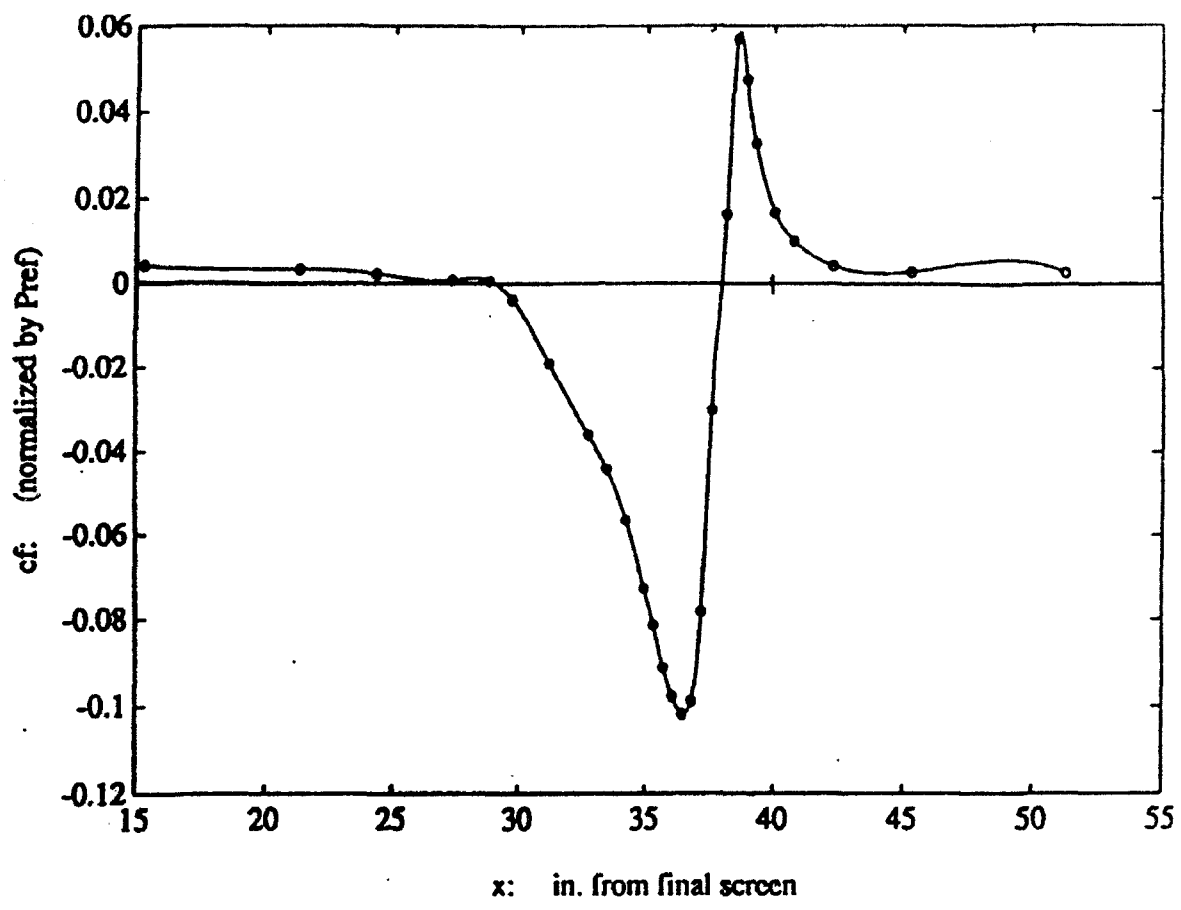


Figure 10. Surface centerline skin friction.

3. NUMERICAL METHODS

The focus of this study is turbulence and its modeling. However, much of the work has been conducted using numerical solutions of the governing flow equations, and the relevant features of the numerical simulation methodology are given here.

Navier-Stokes Equations

All calculations described in this report are based upon numerical solutions of the Navier-Stokes equations in finite-volume form. The discretized solution is represented by \bar{Q} , the average value in a cell volume V , defined by

$$\bar{Q} = \frac{1}{V} \int_V Q \, dV \quad (1)$$

in which

$$\bar{Q} = (\rho, \rho u, \rho v, \rho w, \rho e)^t \quad (2)$$

is the vector of conserved variables, mass, the momenta, and total energy. The conservation law equations for these variables, the "Navier-Stokes" equations, can be written as

$$\frac{\partial}{\partial t} \bar{Q} + \frac{1}{V} \int_S F \cdot dS = 0 \quad (3)$$

in which the surface area of the finite volume is denoted S , dS is the outward surface normal, and F is the flux tensor of the conserved variables:

$$F_x = \begin{bmatrix} \rho u \\ \rho u u + p - \tau_{xx} \\ \rho u v - \tau_{xy} \\ \rho u w - \tau_{xz} \\ u(\rho e + p) - u\tau_{xx} - v\tau_{xy} - w\tau_{xz} + q_x \end{bmatrix}$$

$$F_y = \begin{bmatrix} \rho v \\ \rho u v - \tau_{xy} \\ \rho v v + p - \tau_{yy} \\ \rho v w - \tau_{yz} \\ v(\rho e + p) - u\tau_{xy} - v\tau_{yy} - w\tau_{yz} + q_y \end{bmatrix} \quad (4)$$

$$F_z = \begin{bmatrix} \rho w \\ \rho u w & -\tau_{xz} \\ \rho v w & -\tau_{yz} \\ \rho w w + p & -\tau_{zz} \\ w(\rho e + p) - u\tau_{xz} - v\tau_{yz} - w\tau_{zz} + q_z \end{bmatrix}$$

The thermodynamic pressure is given by

$$p = (\gamma - 1) (\rho e - 0.5\rho(u^2 + v^2 + w^2)) \quad (5)$$

in which $e = c_v T + (u^2 + v^2 + w^2)/2$ is the total internal energy. The viscous and turbulent stresses and the thermal stresses are given in Cartesian tensor notation by

$$\tau_{ij} = (\mu + \mu_t) \left(\frac{\partial u_i}{\partial x_j} + \frac{\partial u_j}{\partial x_i} \right) \quad (6)$$

$$q_j = (k + k_t) \frac{\partial T}{\partial x_j} \quad (7)$$

in which, for example, $\tau_{12} = \tau_{xy}$, T is temperature, μ_t is a modeled turbulent viscosity, and k_t is a modeled turbulent thermal diffusivity.

Equations (1-7) which describe the fluid motion are exact, even when applied on a grid with discrete finite-volume cells. The interpolation and differentiation schemes used to compute the fluxes on the cell faces determine the accuracy of the spatial discretization scheme. These are described below.

Spatial Discretization Scheme

High-accuracy, central, discretization algorithms are described for the finite-volume form of the Navier-Stokes equations in this section. The higher order forms of these methods were developed recently,¹⁰ and no description of them has yet been published. Hence, a summary of the methods is given here.

The integral or finite volume form of the Navier-Stokes equations, Eq. (3) is exact; however, it becomes approximate when numerical approximations are used to compute the fluxes through the faces of the finite-volume cells. Interpolation is used to compute the inviscid fluxes, while finite difference approximations are used to compute viscous fluxes. The inviscid fluxes are the more important of these two, for reasons discussed below.

High-Accuracy Spatial Interpolation - The accuracy of the spatial scheme depends on the accuracy of the interpolation used to determine the values of the cell-face fluxes, based on the volume-average value of the conserved variables in the cells. \bar{Q} is not associated with any specific location in the cell, and specifically, \bar{Q} is not generally the value of Q at the cell center. This fact must be recognized when developing the discretization scheme.

Co-location interpolants which pass through \bar{Q} assigned to the cell centers fail to heed this warning, and they are at best second order accurate. An interpolation scheme based on the assumption that the value at the cell center is the average value will incur an error proportional to $\Delta x^2 \partial^2 F / \partial x^2$. This is the same magnitude error as incurred by a linear interpolation and does not degrade the error of a second order algorithm. If a higher order interpolation scheme is used, it is necessary to account for the nonlinear distribution of the solution within the cell.

In the following equations, a fourth order accurate interpolation scheme will be developed in one space dimension. Fourth order is the lowest order for which special recognition that Q does not coincide with the cell center is required. Following that, interpolation formulae will be given for schemes up to eighth order.

The Navier-Stokes equations can be written in one space dimension as

$$\frac{\partial}{\partial t} \bar{Q} + \frac{A}{V} [F_{j+1/2} - F_{j-1/2}] = 0 \quad (8)$$

in which A is the area of the faces of the finite volume, $F_{j+1/2}$ and $F_{j-1/2}$ are the fluxes at the cell faces, and V is the cell volume. Equation (8) is exact, as is Eq. (3); approximation is introduced, and the spatial accuracy of the scheme is determined by the method used to obtain the cell face fluxes $F_{j+1/2}$ from \bar{Q} .

A simple means of achieving this accuracy is to require that the difference of the interpolants across a cell be equal to a finite difference approximation of the appropriate order. Hence,

$$\frac{\delta F}{\delta x} = \frac{A}{V} [F_{j+1/2} - F_{j-1/2}] \quad (9)$$

must possess desired accuracy, where $\delta F / \delta x$ is the finite *difference* approximation with the desired order of accuracy. From the fourth order finite difference approximation,

$$\delta F / \delta x = (F_{j-2} - 8F_{j-1} + 8F_{j+1} - F_{j+2}) / 12\Delta x \quad (10)$$

the fourth order interpolation is found to be

$$F_{j+1/2} = (-F_{j-1} + 7F_j + 7F_{j+1} - F_{j+2}) / 12 \quad (11)$$

In contrast, the fourth order accurate co-location interpolant which wrongly assumes that \bar{Q} exists at the cell center is given by

$$F_{j+1/2} = (-F_{j-1} + 9F_j + 9F_{j+1} - F_{j+2}) / 16 \quad (12)$$

When differenced, this interpolant yields the approximation of the gradient

$$\delta F / \delta x = (F_{j-2} - 10F_{j-1} + 10F_{j+1} - F_{j+2}) / 16\Delta x \quad (13)$$

whose leading error term is $O(\Delta x^2)$. Hence, Eq. (11) gives the true fourth order accurate representation of the flux at a cell face, which accounts for the variation of Q within the cell's volume.

Formulae for high-order interpolation can be developed, following the approach in Eqs. (9-11), using Taylor series expansions. Central interpolation schemes through eighth order are given in Table 1.

Table 1. Interpolation Weights for $F_{j+1/2}$

	F_{j-3}	F_{j-2}	F_{j-1}	F_j	F_{j+1}	F_{j+2}	F_{j+3}	F_{j+4}	error
$2F_{j+1/2}$				1	1				$O(\Delta^2)$
$12F_{j+1/2}$			-1	7	7	-1			$O(\Delta^4)$
$60F_{j+1/2}$		1	-8	37	37	-8	1		$O(\Delta^6)$
$840F_{j+1/2}$	-3	29	-139	533	533	-139	29	-3	$O(\Delta^8)$

These formulae are based on the assumption of uniform cell sizes, and expressions for stretched grids have not yet been developed. Grid stretching does reduce the accuracy of the interpolation schemes. Therefore, the grid used in the present study are as smooth as practically possible in regions where the solution must be computed with good accuracy.

Spatial Accuracy in Fourier Space - The principal reason for using a discretization method with a high order of accuracy is to minimize the number of grid points needed to accurately represent variations in the solution. Hence, a very relevant means of assessing the accuracy of a method is to determine how few grid points are required to accurately characterize some aspect of the solution. Fourier analysis provides a good means of performing this evaluation.

The shortest wave length λ_0 represented on a grid with a spacing Δx is

$$\lambda_0 = 2 \Delta x \quad (14)$$

which corresponds to oscillations at every other grid point. The equivalent highest wave number is

$$\omega_0 = \pi / \Delta x \quad (15)$$

A numerical discretization scheme will give accurate derivatives up to some "cutoff" wave number $\omega_c < \omega_0$, beyond which the accuracy falls rapidly. ω_c depends on the derivative being computed (e.g., first, second), the level of accuracy required, and, of course, the discretization scheme.

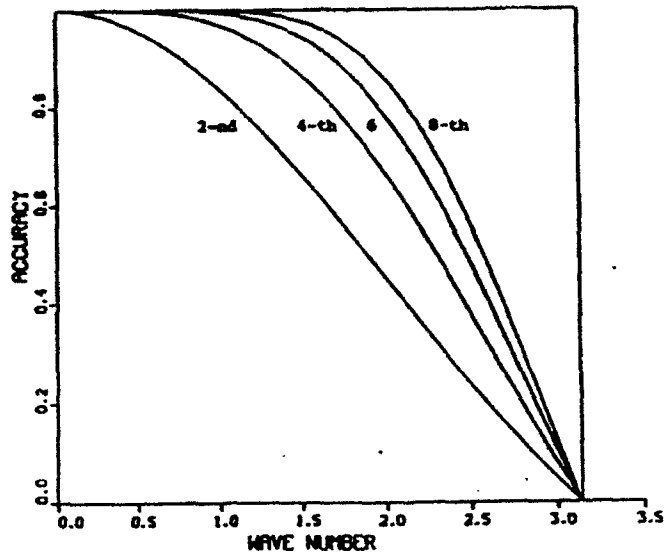


Figure 11. Accuracy of spatial discretization, defined in Eq. 16.

The results of a Fourier analysis of the schemes represented in Table 1 are given in Figure 11.¹⁰ A trial function $F = \sin(\omega x_i / \Delta x)$ is used. The measure of accuracy is:

$$\text{Accuracy} = \frac{\delta F / \delta x}{\partial F / \partial x} \quad (16)$$

in which $\partial F / \partial x$ and $\delta F / \delta x$ are the values of the derivative computed exactly and with the discretization formulae. Derivative terms are computed from the interpolation formulae using Eq. (9). All interpolation schemes in Table 1 have 100% accuracy as $\omega / \omega_0 \rightarrow 0$ and zero accuracy as $\omega / \omega_0 \rightarrow 1$. However, the higher order schemes have nearly perfect accuracy to a much higher wave number than the lower order schemes. The second order scheme is better than 99% accurate up to a cutoff wave number of about $\omega_c = 0.05 \omega_0$, while the eighth order scheme is 99% accurate to about $\omega_c = 0.4 \omega_0$.

In this comparison, the eighth order scheme requires roughly 1/8th as many grid points in each spatial direction for the same accuracy as the second order scheme, or 1/500th as many grid points in a three-dimensional calculation.

Artificial Dissipation - The central discretization schemes described above are non-dissipative. That is, energy cannot be dissipated by numerical discretization of the inviscid fluxes. These schemes permit high wave number oscillations in the solution, which are non-physical and can cause the solution to diverge if they are not regulated. An eighth order nonlinear dissipation scheme is used to remove energy from the high wave numbers in the solution. Because the dissipation is of high-order, low-wave numbers, roughly $\omega < \omega_0 / 2$, are unaffected by the dissipation and computed with good accuracy. This nonlinear scheme was developed in conjunction with the high-order discretization scheme¹⁰ for numerical problems in computational aeroacoustics. The present simulations deal with subsonic flows, and the shock-capturing capabilities of the dissipation are not needed.

Viscous Fluxes - The viscous fluxes at the cell faces are computed with second order central difference approximations. The specific difference approximation used depends

upon the flux required and its location on the grid cell. Let the subscripts j and k denote the indices in the x - and y -directions. Then, for example, the x -gradient term on the cell face between the j and $j+1$ cells is computed as

$$\delta u / \delta x |_{j+1/2,k} = (u_{j+1,k} - u_{j,k}) / \Delta x \quad (17)$$

A y -derivative term computed at the same location is more complex because it must be computed at the j and $j+1$ cell centers and then averaged to the cell face.

$$\delta u / \delta y |_{j+1/2} = (u_{j,k+1} - u_{j,k-1} + u_{j+1,k+1} - u_{j+1,k-1}) / 2\Delta y \quad (18)$$

Equation (17) is more accurate than (18) because the difference is taken over a shorter interval. In general, the most important viscous fluxes are computed with Eq. (17).

The accuracy of Eq. (17), when substituted into the Navier-Stokes equations, has been evaluated using Fourier analysis, as described in the previous section. The second order viscous terms are relatively close in accuracy to the fourth order approximation of the inviscid fluxes in the lower half of the wave number spectrum. Hence, the second order viscous fluxes are comparable in accuracy to the fourth order for inviscid fluxes.

The fourth order interpolation scheme was used for the Reynolds-averaged calculations, because comparable accuracy in the viscous and inviscid terms is appropriate. The eighth order scheme was used for the large eddy simulations which are convection-dominated.

Boundary Conditions - A wide variety of boundary conditions are required to perform the range of calculations in this study. In general, standard boundary condition methods are used, and a relatively brief description of these is provided here. Although the calculations are performed with the finite volume method, the boundary conditions are imposed on the solution variable \bar{Q} rather than on the fluxes.

The impingement wall is treated with no-slip adiabatic conditions, and therefore,

$$u = v = w = \partial \rho / \partial y = \partial p / \partial y = 0 \quad (19)$$

in which y is normal to the wall. One-sided, second order approximations are used to compute the derivatives at the wall, so the boundary values are computed with an extrapolation expression,

$$\rho_1 = 1.333\rho_2 - 0.333\rho_3 \quad (20)$$

in which the subscript $()_1$ denotes the boundary values and others are interior values. However, the shear stress between the first and second grid points, effectively the wall shear stress, is computed with "wall functions." A logarithmic law-of-the-wall velocity profile is assumed to exist between the wall and the first interior grid point, and the shear stress is computed to be consistent with this profile. The velocity at the first interior point is restrained only by this shear stress, and not by the artificial dissipation; hence, that velocity can be large. Tunnel side and top walls were treated with an impermeable slip boundary condition.

The non-reflecting boundary conditions developed by Thompson,¹¹ with some modifications, are used for the non-wall boundaries, which included the inflow, outflow, and occasionally the top boundaries. These are briefly summarized here, using finite difference notation for compactness. The equations for one-dimensional flow can be written in nonconservative form as

$$\frac{\partial Q}{\partial t} + A \frac{\partial Q}{\partial x} = 0 \quad (21)$$

in which A is the Jacobian matrix of the inviscid flux vector. Through eigenvector-eigenvalue manipulations, the A matrix can be split into two matrices which have positive and negative eigenvalues, $A = A^+ + A^-$. They represent the information which propagates in the +x and -x directions, respectively. Upwind differencing consistent with the direction of signal propagation is then used to compute spatial gradients, and Eq. (21) becomes

$$\frac{\partial Q}{\partial t} + A^+ \frac{\delta^+ Q}{\delta x} + A^- \frac{\delta^- Q}{\delta x} = 0 \quad (22)$$

Under the assumption that no information enters the domain through a boundary, it is appropriate to discard the A^- term at the x_{\max} boundary and the A^+ term at the x_{\min} boundary because these terms represent incoming information. The boundary conditions are applied by integrating Eq. (22) with either A^+ or A^- set to zero at the boundary points plus the full spatial gradient terms in the other spatial directions.

It was necessary to modify the Thompson boundary conditions at several boundaries. With no incoming information it is not possible to control the ambient pressure. This difficulty is resolved by letting the boundary pressure relax slowly to the selected ambient pressure. At each time step, the boundary pressure was typically made up of 99% of the pressure computed with Thompson's boundary conditions and 1% of the ambient pressure at each application of the boundary conditions. Hence, a characteristic time for the relaxation to ambient pressure was 100 time steps. Since this change in pressure is physically caused by incoming acoustical waves which are isentropic, the density is adjusted to preserve the entropy at the boundary. The velocities at a subsonic inflow boundary are also imposed by computing the boundary velocities as a weighted average of the values computed with the Thompson boundary conditions and the imposed mean values, with similar weights to those used for the pressure. Hence, the inflow velocity could deviate from the desired value during transients in the calculation, but it would asymptote to the correct value in the steady-state solution.

Turbulent Inflow Boundaries - The boundary layer flow at inflow boundaries was specified from experimental data, when available. Typically, the only data available from the freestream boundary layers were mean velocity profiles or total thickness. Data from Cimbalá¹² indicate that the dominant characteristics of impinging jet flows depend only weakly on the boundary layer thickness. In the calculations, a $y^{1/7}$ velocity profile was used for the mean velocity, and the turbulence was assumed to be that of a flat plate boundary layer. The turbulence energy k was taken from typical flat plate data, and ϵ was set to give the correct shear stress, given k and the velocity profile.

For the primary test case, the jet flow issued from a long constant-diameter pipe and was nearly fully developed. The measured velocity profile, including the measured deflection from straight flow, was used. Turbulence was assumed to be from a fully developed pipe flow at the appropriate Reynolds number.

Large Eddy Simulation Inflow Conditions - Boundary conditions used for LES are similar to those for mean flow calculations, except at the jet exit. Here, the velocity field must approximate a turbulent pipe flow. Two attempts were made to obtain a reasonable turbulent inflow.

In the first effort, an auxiliary calculation was performed of homogeneous, isotropic turbulence. This solution was stored and used to provide turbulence which was added to the mean inflow velocity field. This approach should have given a reasonable boundary condition for jet exit flow, but the simulation in which it was used was unsuccessful. The major shortcomings in that simulation are believed to be due to factors other than the boundary conditions. The simulation was run early in the contract effort with fourth order spatial discretization (the eighth order scheme had not yet been developed), and the grid may have been too coarse.

The second effort used a random number generator to specify the turbulent fluctuations:

$$\begin{aligned}u' &= u_0 \text{RANF } f(r) \\v' &= u_0 \text{RANF } f(r) \\w' &= u_0 \text{RANF } f(r)\end{aligned}\tag{23}$$

in which u_0 was a turbulent scaling velocity, typically about 10% of the jet maximum velocity, RANF is the Cray random number generator, and $f(r)$ was a function with maximum value of unity which confines the fluctuations to the jet's shear layer. These turbulent fluctuations were added to the mean velocity and the combined velocity was imposed at the nozzle exit. This form of "inflow turbulence" is entirely non-physical, and it contains no inherent structures. However, it contains turbulence energy in all three velocity components, and it provides a "seed" from which natural turbulence can evolve.

Note that imposed perturbations at the nozzle exit are not required to generate an unsteady simulation. In a study by one of the present authors,¹³ steady nozzle exit conditions were used for a subsonic impinging jet simulation, and that flow became unsteady. The acoustical energy emanating from the impingement region is sufficient to perturb the jet shear layer at the nozzle exit and produce a turbulent flow. However, with the limited resolution employed in three-dimensional simulation, the secondary instabilities which lead to three-dimensional turbulence may be artificially suppressed by numerical errors. Thus, the simulated turbulence which occurs without random forcing is prone to be less realistic than that with the forcing.

The validity of using random forcing to replace the inflow turbulence is subject to question. However, the results seem to suggest that they are adequate.

Time Integration - A five-stage second order accurate Runge-Kutta scheme developed by Mavriplis and Jameson¹⁴ is used to advance the equations in time. This

scheme is explicit but is relatively stable and permits the use of CFL numbers up to ~ 2.8 with the present space discretization. The time step can be spatially variable if a calculation is being run to a steady state, as in the case of Reynolds-averaged calculations. When time accuracy is required for large eddy simulations, the time step is fixed, and the maximum CFL number is typically less than unity to provide good temporal accuracy.

4. LARGE EDDY SIMULATIONS

The physical processes which control turbulence in impinging jets are poorly understood, as noted in the introduction. The best experimental measurement techniques currently available cannot provide the information needed to identify these processes. Hence, an alternate approach is required, and large eddy simulation (LES) is used in this study. As its name implies, LES involves flow simulations which resolve the large scales of turbulence in addition to the mean flow. LES can be used to obtain reasonable approximations of the dominant physical processes in complex flows such as impinging jets.

LES employs the Navier-Stokes equations as the model of the resolved portion of the flow. The eighth order spatial scheme and the Runge-Kutta time integration, described previously, are used to integrate these equations.

The small scales of turbulence are not resolved in LES, and they must be approximated with some form of model. Numerous sub-grid-scale (SGS) turbulence models have been proposed, and they are generally demonstrated in flow such as boundary layers or homogeneous turbulent flows. To the present authors' knowledge, no SGS model has been validated for turbulence similar to that in impinging jet flows. This is a significant point because the dominant turbulent structure in the impinging jet region consists of quasi-axisymmetric vortical structures.¹² It is important, therefore, that the SGS model accurately predict the stresses in these vortices. Unfortunately, simple models are notoriously inaccurate for complex vortical flows, and typical SGS models will be poor for LES of impinging jet flows.

No explicit SGS model is employed in the present large eddy simulations. Instead, the artificial dissipation operator produces diffusive transport, which mimics small scale turbulent mixing, at the highest resolvable wave numbers. The artificial dissipation is fairly specific to the highest wave numbers that can be supported on the grid; this permits the simulation to capture the widest possible range of turbulent scales. The larger resolved scales of turbulence are unaffected by the artificial dissipation.

LES Cases - Two flows were studied with LES: a normal impinging jet, and an inclined impinging jet at conditions similar to the primary experimental test case. In the normal impinging jet, the region of "interesting" physics is confined to the impingement zone and the initial part of the radial wall jet. Since this region is relatively compact, it is possible to use a grid which gives good numerical resolution in this region, while the grid can be coarser toward the outer boundaries. In calculations of the inclined impinging jet, the grid must have roughly uniform grid spacing throughout the entire ground vortex, which is a large region. This requirement significantly increases the computational cost and difficulty, and reduces the accuracy which can realistically be achieved. Hence, the case of the normal impinging jet provides a better understanding of turbulence physics than the inclined jet case. The simulation of the inclined jet does reveal differences between the two flows which are critical for turbulence modeling. The operating conditions of the simulated inclined jet differs from the experiment. The simulated Reynolds number is lower because the grid resolution which can realistically be afforded is inadequate for a higher Reynolds number. The jet exit Mach number, M_j , cannot be made as small as the experiment because the stability limit on the computational time step makes low Mach number simulations very expensive. Jet Mach numbers in the range $0.4 < M_j < 0.5$ are low enough so that

compressibility and aero-acoustic effects on the turbulence will be negligible. Neither difference should materially affect the conclusions obtain from the simulation results.

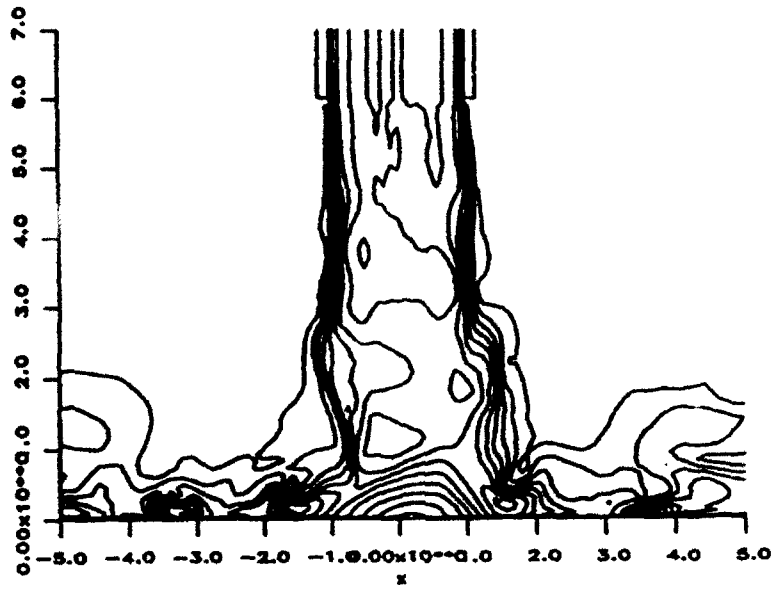
The configuration for the normal jet LES is $H_j/D_j = 3$, $M_j = 0.4$, and $Re_D = 50,000$. The jet-exit boundary layer thickness is $\delta/D_j = 0.1$. The inclined jet case is run at $H/D = 3.1$ and $\phi = 45^\circ$, which is the same as the experiment. However, $Re_D = 50,000$ and $M_j = 0.5$. The jet exit flow has the same boundary layer thickness as the experiment, and the turbulence energy and dissipation rate are appropriate for a turbulent pipe flow.

Dynamical LES Results for Normal Impingement - LES generates large quantities of data, and, at present, only a fraction of that data can be processed or included in a report. The results presented here have the specific purpose of illustrating the physical processes which are critical to turbulence and which must be modeled accurately.

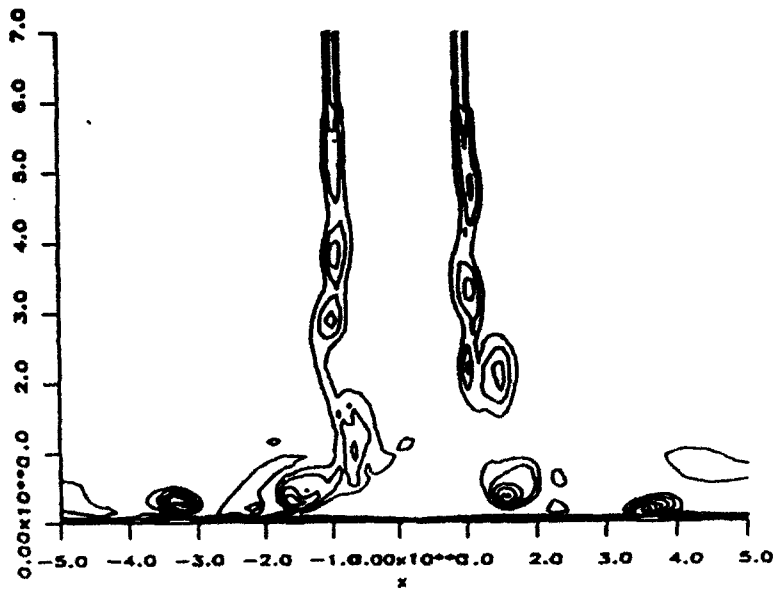
The dynamical results are presented first because they provide good insight into the physics of turbulence. Mach number contours on a plane through the centerline of the jet are given in Figure 12-a. The jet exits the nozzle with a relatively thin shear layer and without any large eddy structure. At one-half the distance to the impingement plate, the jet shear layer has developed significant structure, which increases down to the impingement plate and in the wall jets. The maximum Mach number does not occur in the free jet, but rather in the wall jet near $x = 3.5$. This is a somewhat surprising result, but readily explained by the dynamics of turbulence

Contours of vorticity magnitude on the same plane are given in Figure 12-b. The relatively uniform shear layer near the nozzle exit appears as a continuous sheet of vorticity which then forms discrete vortices. The vortices pair before they strike the ground. Vortices in the wall jet are seen at $x = \pm 3.5$. These are smaller and have higher levels of vorticity than the vortices in the jet above the impingement plate, despite the fact that they are older and would therefore be larger and weaker due to the diffusion of vorticity. Some process causes the vortices to intensify in the wall jet.

This impinging jet flow is axisymmetric in the mean. Turbulence in the jet consists of filaments of vorticity. These filaments are not randomly oriented, but rather tend to form rings that enclose the jet. Hence, they are quasi-axisymmetric in the free jet and tend to preserve that structure for some distance into the wall jet. Also, they convect with roughly half of the local jet velocity. When these vortex filaments flow outward in the wall jet, their major diameter increases at a rate roughly equal to $U_j/2$. By conservation of mass, this stretching of the major diameter causes the minor diameter, the thickness of the vortex filament seen in the figure, to decrease. The vorticity must also increase to satisfy the conservation of angular momentum. A time series of vorticity contours given in Figure 13 indicates that the peak vorticity may triple as the vortices flow outward in the wall jet.



(a) Mach number



(b) Vorticity magnitude

Figure 12. Contours of Mach number and vorticity magnitude for normal impinging jet.

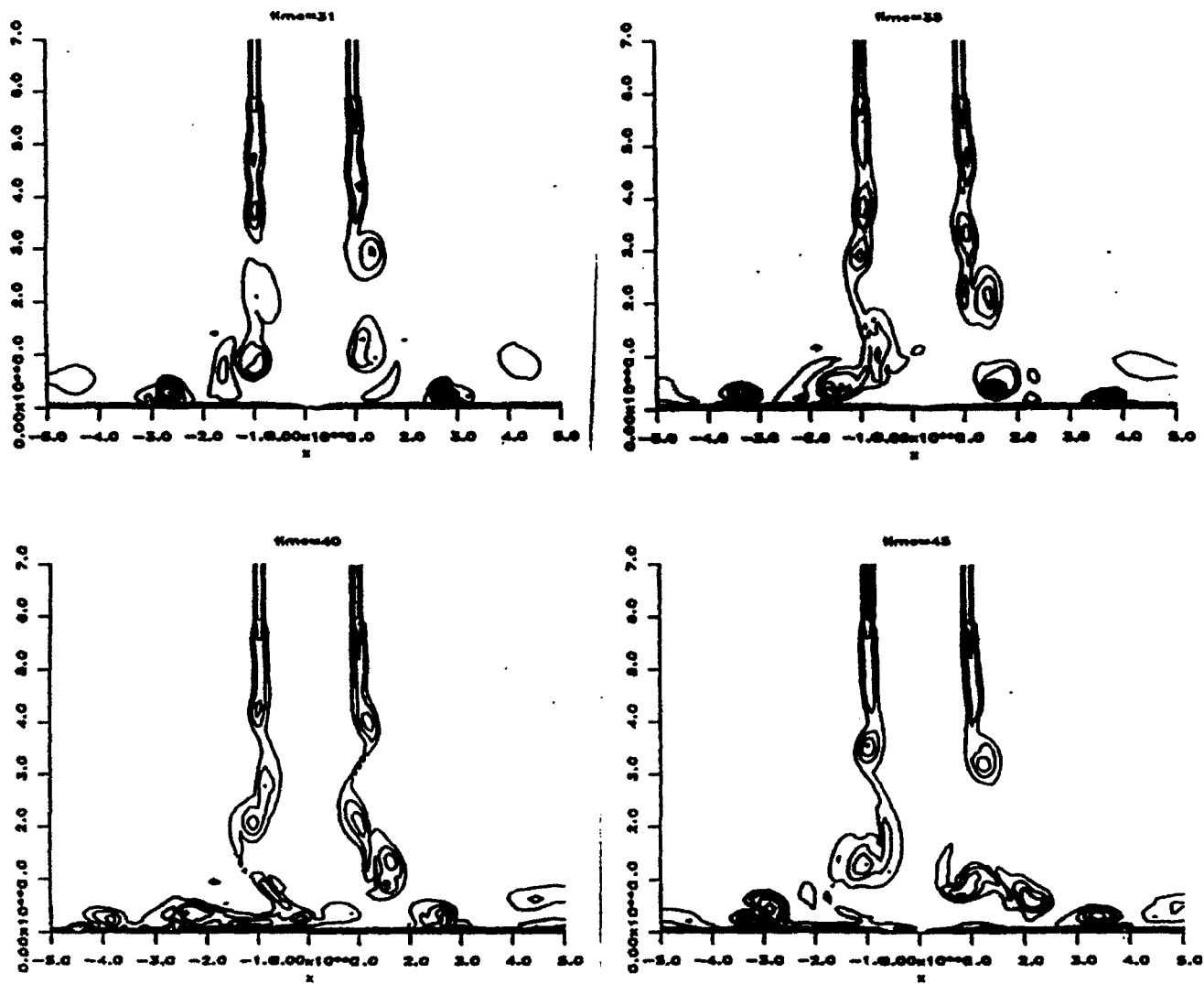
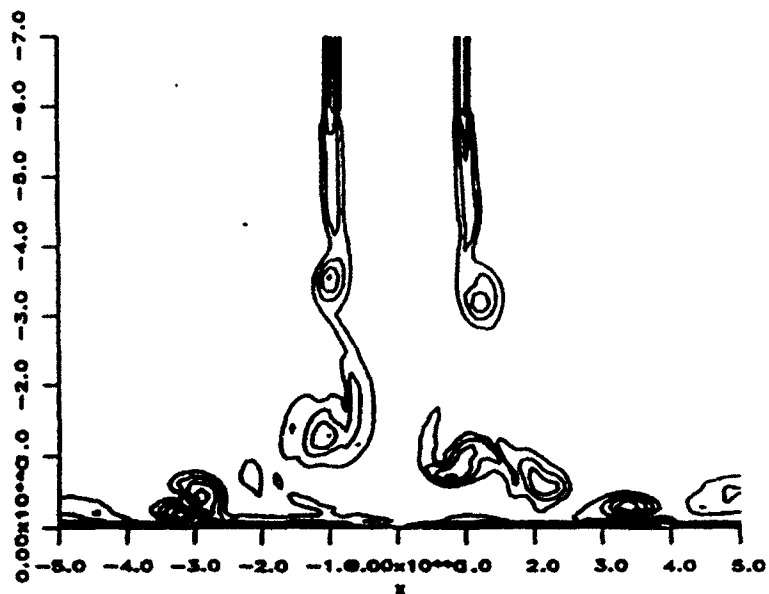
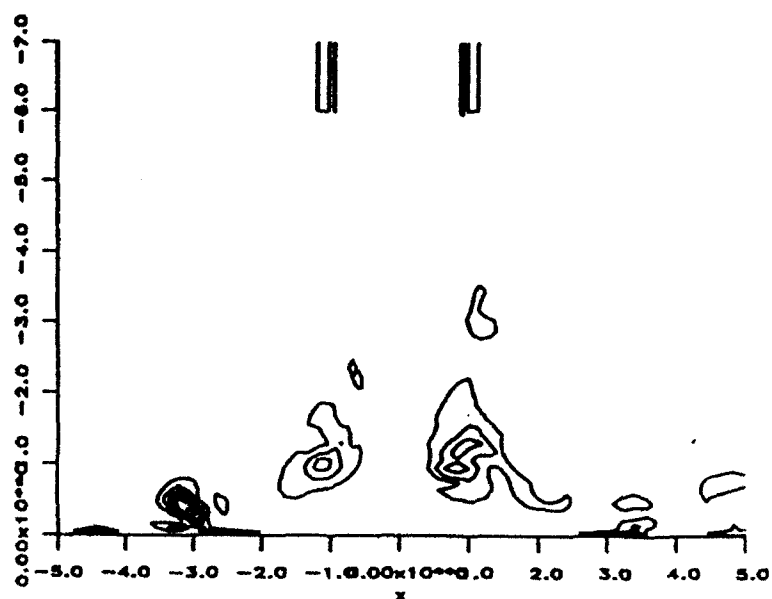


Figure 13. Time sequence of vorticity contours for normal impinging jet.

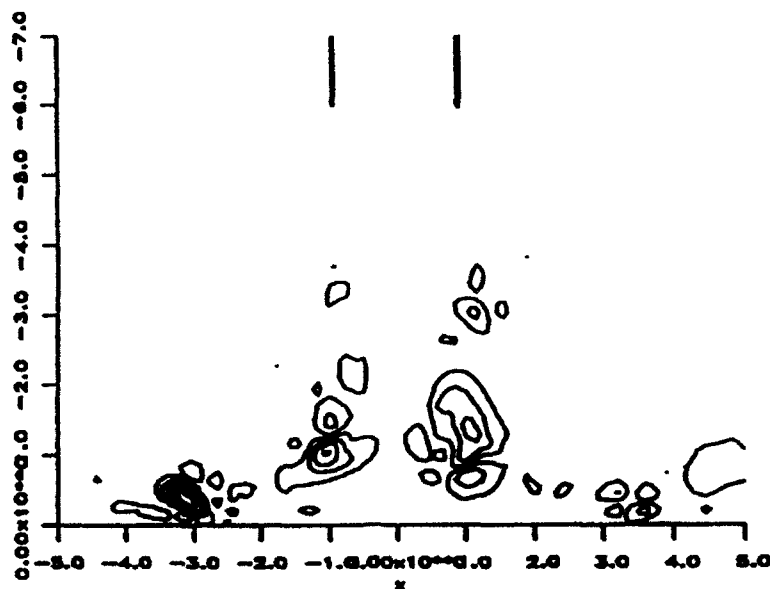
In addition to increasing the peak vorticity, vortex stretching can increase the shear stress. The instantaneous velocity fluctuations can be computed by subtracting the mean velocities from the instantaneous velocities; the instantaneous turbulent stresses are then given by the product of two fluctuating velocities. Figure 14 gives the instantaneous vorticity, turbulence energy $(u'u' + v'v' + w'w')/2$ and the shear stress, $u'v'$. The peaks of energy and shear stress are associated with the vortices: as expected, the turbulent stresses are carried by the vortices. The maximum values of energy and shear stress at this instant are larger in the wall jet than in the free jet. This trend also applies to the time-averaged shear stress as shown in statistical results presented below.



(a) Vorticity



(b) Turbulence energy



(c) Shear stress

Figure 14. Contour plots on instantaneous vorticity, turbulence energy $(u'u' + v'v' + w'w')/2$ and the shear stress, $u'v'$.

Hence, vortex stretching is a critical mechanism which affects turbulence in the impingement region, particularly in the wall jet flowing away from the impingement point.

It is reasonable to question whether the above implication of vortex stretching as a critical turbulence mechanism results from approximation used in the numerical simulation method. The importance of vortex stretching would be over-emphasized in a simulation which is axisymmetric. Therefore, it is important to establish the three-dimensionality of the flow, both in the free jet and in the wall jet. Figures 12 and 13 show that the free jet is not symmetric about its centerline. Figure 15 give the instantaneous Mach number contours on a plane normal to the free jet, and again, significant highly three-dimensional structures can be seen. A top view of Mach number contours and velocity vectors in the wall jet ($y = 0.3$) in Figure 16 also shows that the flow is very much three-dimensional; however, a dominant quasi-axisymmetric structure does exist. The velocity vectors suggest that the three-dimensionality increases with increasing radius. These results demonstrate that three-dimensional turbulence exists in the simulations. This suggests, but does not prove, that the vortex stretching mechanism is not artificially augmented by the limited resolution available in the simulation.

Dynamical LES Results for the Primary Test Case - A large eddy simulation was also performed of the primary test case. As mentioned above, the magnitude of this calculation was significantly greater than the normal impinging jet. The calculation was performed on a grid which had less resolution than the previous case, and the time scale of the global flow field was significantly longer than the flow in just the impingement region. This calculation was not run long enough to obtain statistics. However, information concerning the dynamical structure of turbulence was obtained, which provides insight into the important vortex stretching process.

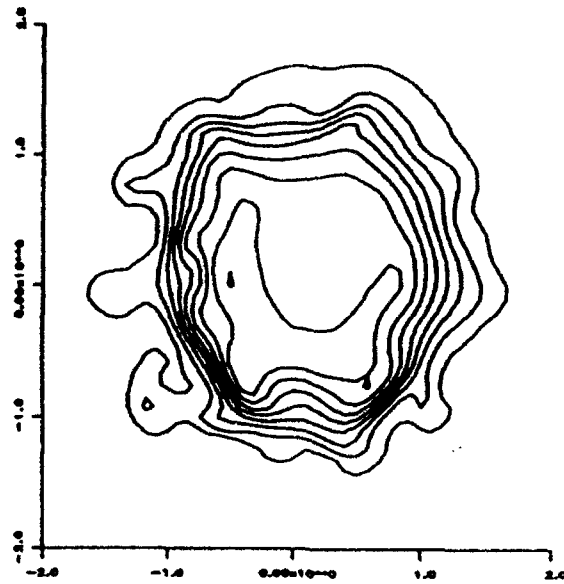
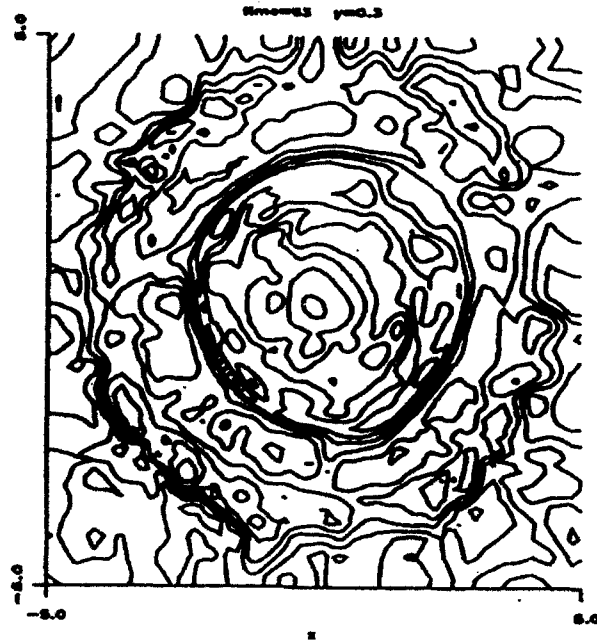
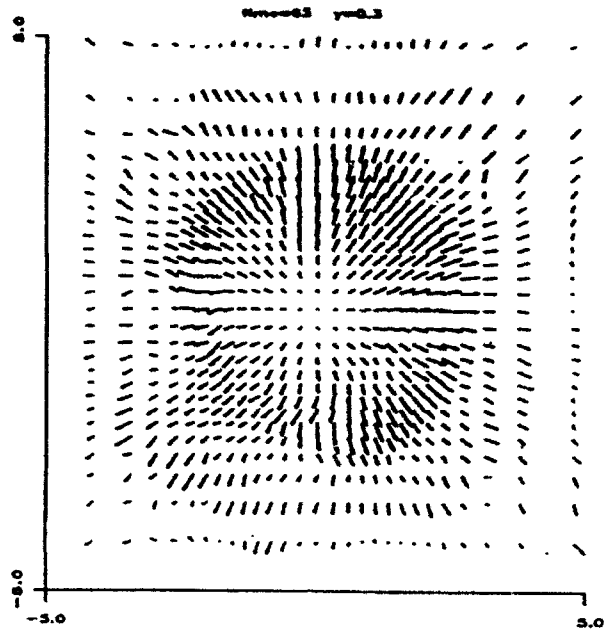


Figure 15. Instantaneous Mach number contours on a plane normal to the jet and above the impingement zone, for the normal impinging jet.

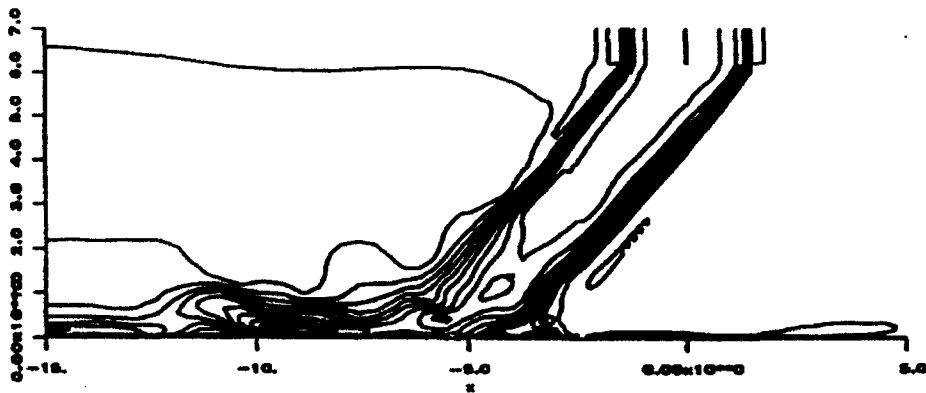


(a) Mach number

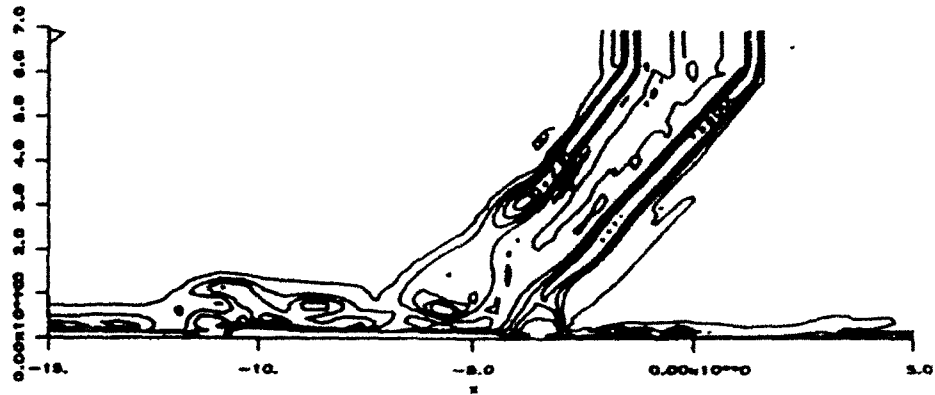


(b) Velocity vectors

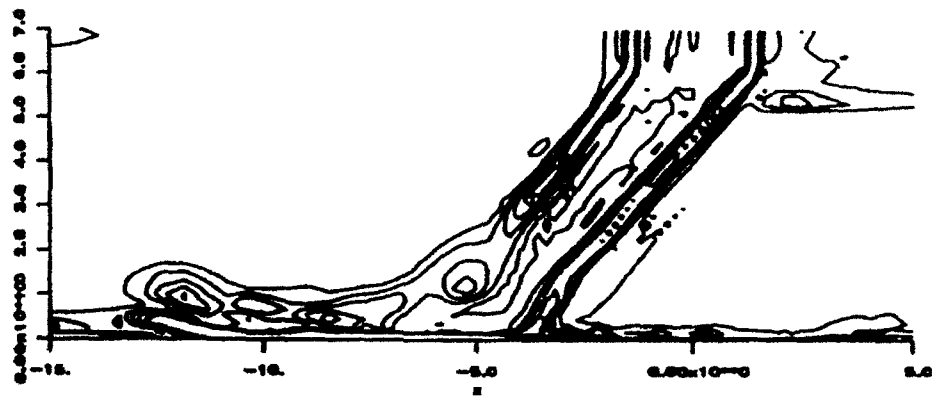
Figure 16. Top view of instantaneous Mach number contours and velocity vectors at $y = 0.3$, for normal impinging jet case.



(a) Mach number



(b) Vorticity magnitude, time = 55



(c) Vorticity magnitude = 64

Figure 17. Contours of Mach number and vorticity magnitude on the center plane for inclined jet case, and vorticity contours at a later time showing vortex evolution.

Figure 17 gives Mach number and vorticity magnitude contours on the centerplane through the jet pipe and ground vortex at one instant in time. The Mach number contours reveal the general location of the jet shear layers, and the fact that the majority of the jet fluid goes forward into the ground vortex. The dynamical structure due to turbulence is not as pronounced as in the normal impinging jet case, perhaps because of the reduced grid resolution. As in the case of the normal impinging jet, vortex stretching amplifies the peak vorticity and decreases the vortex size in the wall jet. Vorticity contours in Figure 17-b and, at a later time in Figure 17-c, reveal several discrete vortices. The vortices upstream of the impingement point ($x \lesssim -5.0$) are comparable in strength to, or weaker than, the peak

vorticity in the jet shear layer. Comparison of Figures 17-b and 17-c reveals that vortices do intensify in this region; however, the peak vorticity is significantly less amplified than in the normal impingement case. Downstream of the impingement point several compact, intense vortices can be seen. The peak turbulent vorticity in Figure 17-c occurs in the wall jet at $x = -2.5$. (This figure also reveals the scale of vortices that can be resolved on this grid.) A top view of the velocity vector field is given in Figure 18. The lateral divergence, $-\partial w / \partial z$, appears to be stronger downstream of the impingement point than upstream of it. This characteristic of the mean flow causes the different amplification of vortices upstream and downstream of the impingement zone.

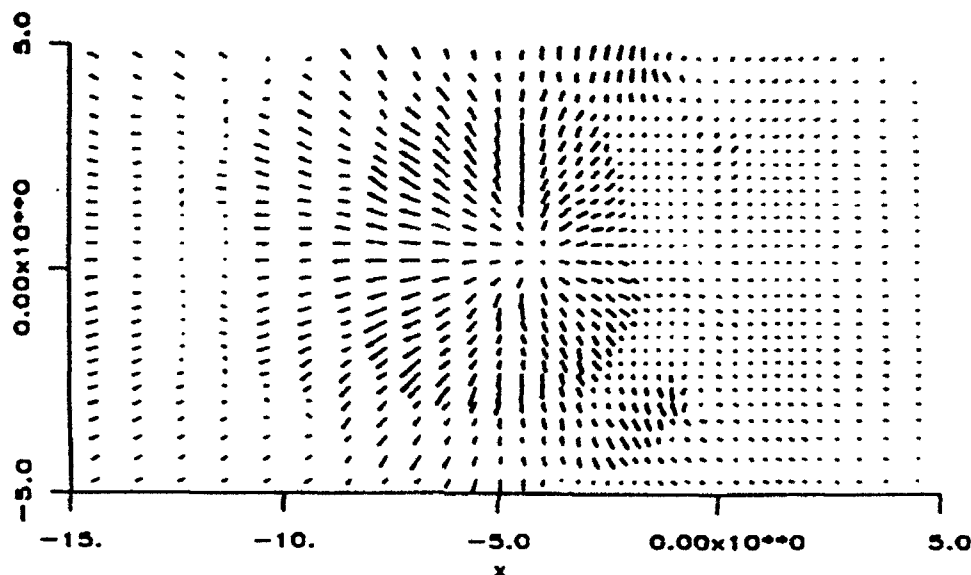


Figure 18. Velocity vectors at $y = 0.03$ (at every other grid point) showing lateral divergence, $-\partial w / \partial z$, in regions of vortex intensification.

Statistical Results for Normal Impingement - In order to obtain turbulent statistics, the turbulence simulation was run until it appeared to have reached an asymptotic unsteady condition, independent of its initial conditions. Integration was then started to obtain time-averages of various flow variables. This integration was performed over a reasonable length of time, until the turbulent statistics computed from these averages demonstrated clear trends. In these simulations, the integration was not carried out long enough to obtain converged statistics because the computational cost would have exceeded the available CPU time. For this flow which is steady and axisymmetric in the mean, the turbulent statistics should display an appropriate symmetry about the jet centerline. As will be seen below, the results are not symmetrical because the statistics are not converged. However, the integration time was sufficient to obtain an understanding of the dominant physical characteristics of impinging jet turbulence, and to identify some critical differences between normal and inclined impinging jets.

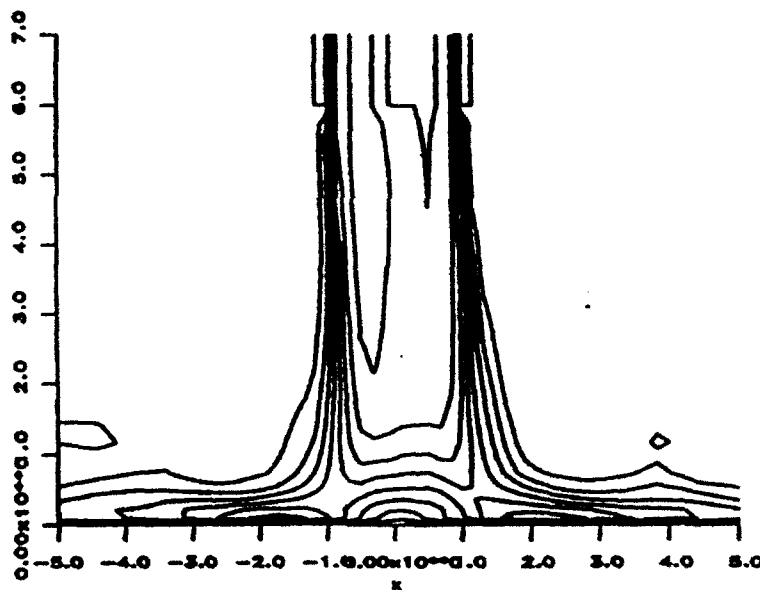
These impinging jet flows are three-dimensional in the mean. Averages are computed with respect to time; there are no spatial directions in which the mean flow or turbulence is homogeneous so that spatial averaging can be used in addition to temporal averaging. The

calculation of turbulent statistics requires a large amount of memory and integration time. To reduce the memory requirements, the statistics are computed at every other grid point in each spatial direction; this reduces the memory required for the statistics calculation by a factor of 8. Time averages were obtained from the simulation which permitted the calculation of the following statistics:

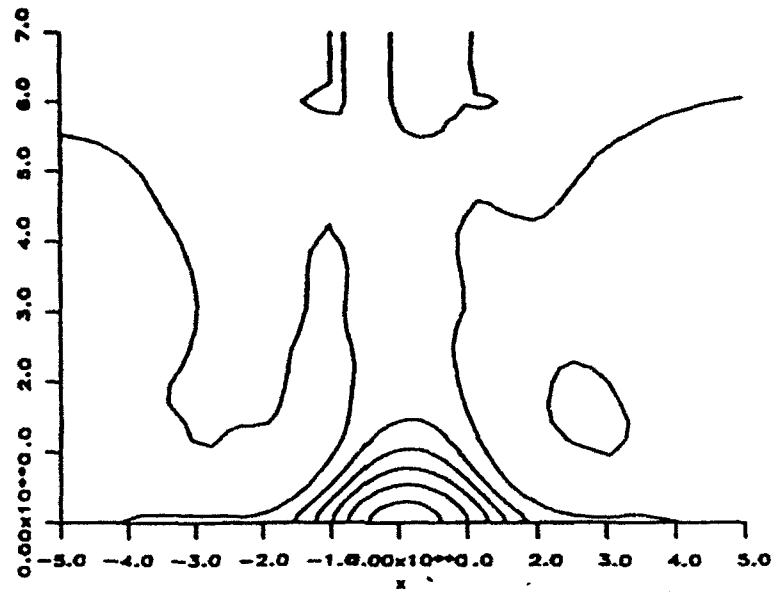
$\overline{\rho, u_i, p}$	mean variables
$\overline{u_i u_j}$	turbulent stresses
$\overline{p \partial u_i / \partial x_j}$	pressure strain correlation

which are believed to be the quantities of greatest importance in these flows.

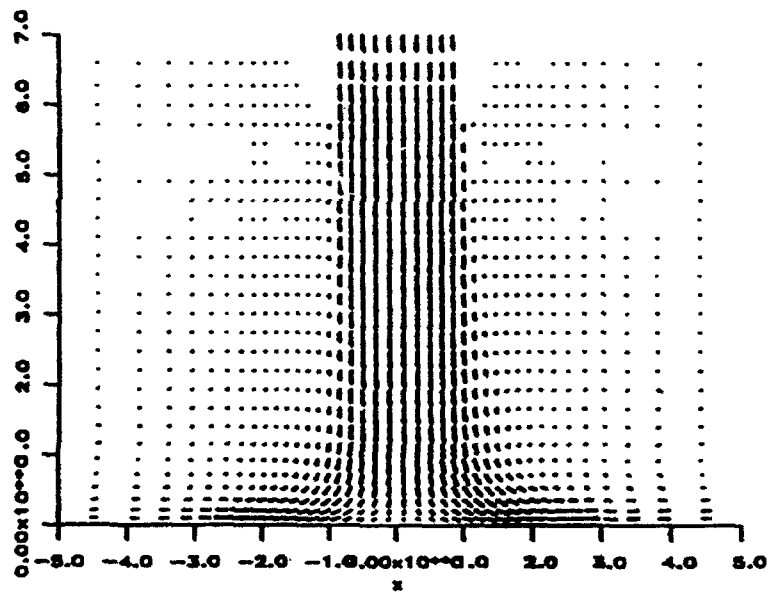
The simplest statistics are the mean flow quantities, and the mean Mach number and pressure contours and the velocity vectors are given in Figure 19. Qualitatively, these results are similar to results from a conventional Reynolds-averaged calculation.



(a) Mach number



(b) Pressure contours

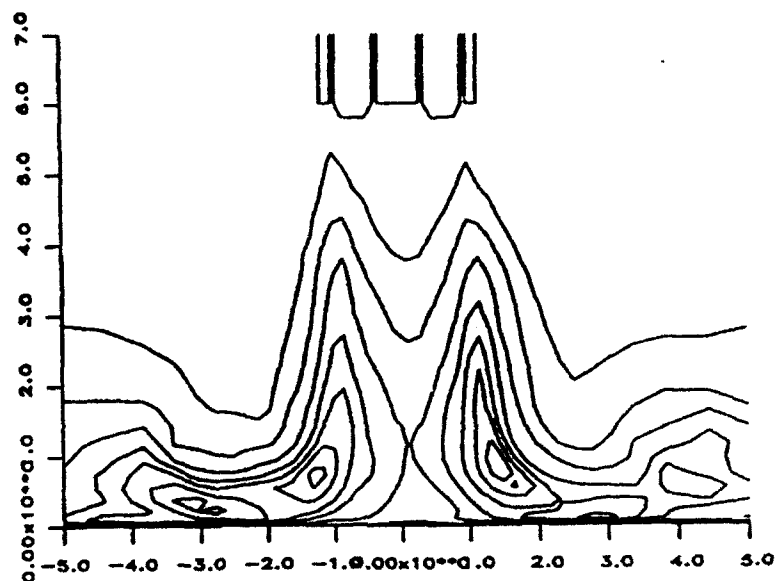


(c) Velocity vectors

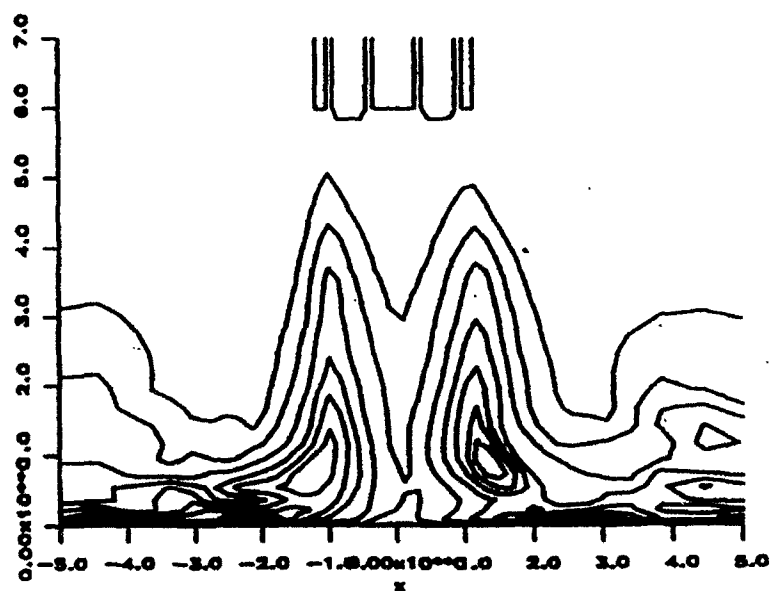
Figure 19. Mean Mach number and pressure contours, and velocity vectors on center plane of normal impinging jet, computed from time average of LES results.

Contours of turbulence kinetic energy on a plane through the center of the jet are given in Figure 20-a. The turbulence energy is below the minimum contour level at the nozzle exit but increases rapidly in the shear layers of the free jet. The peak energy is reached in the impingement zone and remains relatively large in the wall jet. The $u'u'$ and $v'v'$ normal stresses in Figure 20-b and 20-c reveal significantly greater spatial variations than the

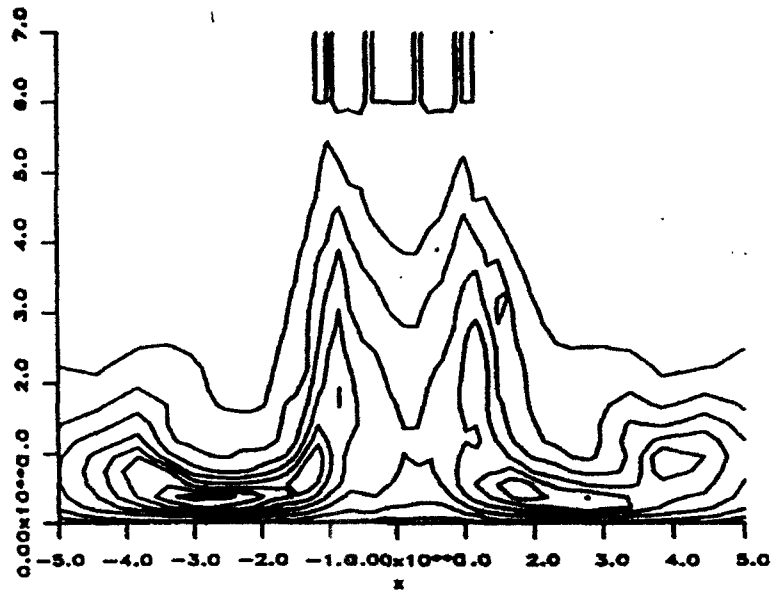
turbulence energy in the impingement zone. The $\overline{u'u'}$ (which is parallel to the wall) has local maxima very near the wall, beneath the wall jet, and in the impingement zone. The maximum $\overline{v'v'}$ values also occur in the wall jet, but somewhat above the wall at a location that corresponds roughly with the vortex cores seen in Figures 12 and 13. The shear stress, given in Figure 20-d, also reaches its maximum values in the wall jet at about the same locations as the maximum in $\overline{v'v'}$. These results further emphasize the relation between unsteady vorticity and the turbulent stresses, and hence, the significance of vortex stretching as a means of increasing shear stress in the wall jet.



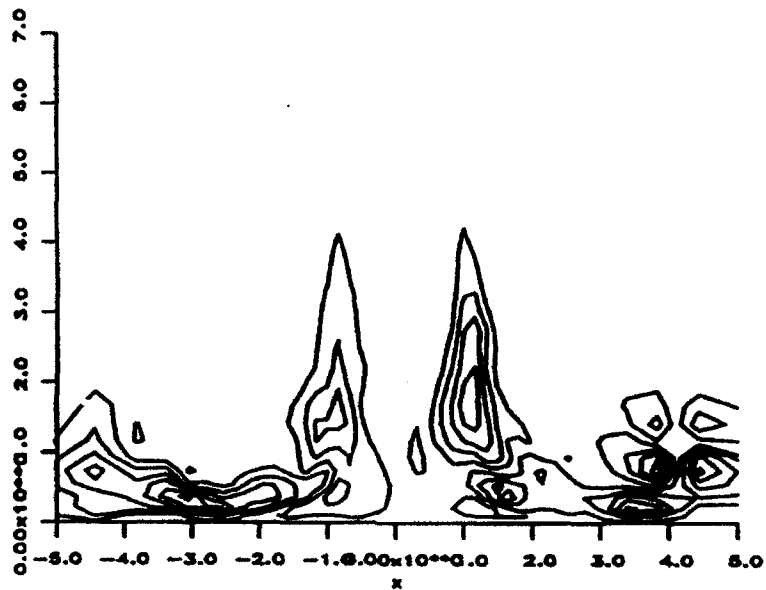
(a) Turbulent kinetic energy



(b) Normal stress, $\overline{u'u'}$



(c) Normal stress, $\overline{v' v'}$



(d) Shear stress, $\overline{u' v'}$

Figure 20. Contour plots of turbulent statistics on center plane of normal impinging jet, computed from time average of LES results.

There is also a tendency for the shear stress to increase in the wall jet while the turbulence energy does not. The correlation coefficient $R_{12} = \overline{u'v'} / (\overline{u'u'} \overline{v'v'})^{1/2}$ is also larger in the wall jets than in the free jet. These results indicate that some process in the wall jet, presumably vortex stretching, causes turbulence there to be more efficient at producing shear stress from the available turbulence energy. This has important implications for turbulence modeling, because it implies that vortex stretching can cause the shear stress to increase without increasing the turbulence energy. Vortex stretching modifications to the $k-\epsilon$ model should therefore be directed principally at the ϵ -equation. However, consideration of the Reynolds-stress transport equations indicate that this is not strictly so.

In summary of this section, the LES results have provided dynamical and statistical information about impinging jet turbulence. Both viewpoints indicate that vortex stretching is a critical process in the wall jet which emanates from the impingement region. Vortex stretching intensifies vorticity fluctuations, and certain components of turbulence are also increased. A significant difference between the normal and inclined impinging jets is the magnitude of vortex stretching in the wall jet that flows forward (into the crossflow) from the impingement point. The wall jet from the inclined jet experiences less lateral divergence, and the shear stress is less amplified, than in the normal impinging jet.

5. TURBULENCE MODELING

The k - ϵ model is used for the basis of this work because it is one of the best all-purpose models currently available, because it is relatively easy to use, and because more complex models have not been demonstrated to be superior for impinging jet flows. As noted in the Introduction, many types of turbulence models have been applied to impinging jet flows, and, almost without exception, these models have failed to give adequate accuracy. Modifications to the k - ϵ model which account for the effects of streamline curvature and vortex stretching are described in this section. These modification should also be applicable to many other two-equation eddy viscosity models via a transformation of variables.

The Standard k - ϵ Model

Turbulent stresses are computed via the Boussinesq approximation.

$$\overline{\rho u'_i u'_j} = -\mu_t (\partial U_i / \partial x_j + \partial U_j / \partial x_i) + \delta_{ij} 2\rho k / 3 \quad (24)$$

in which

$$\mu_t = C_\mu k^2 / \epsilon \quad (25)$$

is the eddy viscosity. The k -equation is obtained from the trace of the Reynolds-stress transport equations with an approximation for diffusive transport and is believed to be without major flaws. It can be written as

$$\frac{D\rho k}{Dt} - \frac{\partial}{\partial x_j} \frac{\mu_t}{\sigma_k} \frac{\partial k}{\partial x_j} = P_k - \rho \epsilon \quad (26)$$

in which P_k is the production of turbulence energy derived by contracting the production tensor in the Reynolds-stress transport equations

$$P_{ij} = -\overline{\rho u'_i u'_m} \partial U_j / \partial x_m - \overline{\rho u'_j u'_m} \partial U_i / \partial x_m \quad (27-a)$$

$$P_k = -\overline{\rho u'_i u'_j} (\partial U_i / \partial x_j + \partial U_j / \partial x_i) / 2 \quad (27-b)$$

The ϵ -equation is

$$\frac{D\rho \epsilon}{Dt} - \frac{\partial}{\partial x_j} \frac{\mu_t}{\sigma_\epsilon} \frac{\partial \epsilon}{\partial x_j} = S_\epsilon \quad (28)$$

in which the source term for the standard model is given by

$$S_\epsilon = C_{\epsilon 1} \rho \frac{\epsilon}{k} P_k - C_{\epsilon 2} \frac{\rho \epsilon^2}{k} \quad (29)$$

The ϵ -equation was originally derived from the fluctuating vorticity transport equation. It can also be derived from the Reynolds-stress transport equations for shear stress and energy, using the k - ϵ expression for shear stress, Eq. (24), to obtain the ϵ transport equation. Equations (24-29) define the standard, high-Reynolds number form of the k - ϵ model. Model coefficients are given in Table 1. These equations, with modifications described below, are solved throughout the flow domain except at the wall.

Between the point at the wall and the first interior point, the so-called wall functions are used to approximate the mean flow and turbulence. With the assumptions of incompressible flow, a logarithmic velocity profile, constant shear stress, and turbulence production equaling dissipation, the wall function relations can be derived. (See, e.g., Ref. 15.) These equations give wall boundary conditions for k and ϵ , and the wall shear stress.

The standard k - ϵ model works reasonably well for a limited range of flows, but its accuracy is poor for most complex flows. Modifications which improve the model's accuracy are described below.

Modifications to the k - ϵ Model

An underlying tenet of the present work is that the effects of streamline curvature and vortex stretching are two of the most significant extra strains which occur in impinging jet flows, and which are not treated accurately by the standard k - ϵ model. If the turbulence model can be modified so that it performs well for these phenomena, for fundamentally correct reasons, it should also perform well in complex impinging jet flows.

Streamline Curvature - There is a considerable body of research dealing with the effects of streamline curvature on turbulence.¹⁶⁻²⁰ The present model is similar to the one proposed by Launder et al.¹⁸ At the heart of the curvature model is the curvature stability parameter β which indicates whether the additional strains due to streamline curvature promote or suppress turbulence. For a simple curved flow

$$\beta = -(2V/R)(\partial V/\partial n + V/R) \quad (30)$$

in which V is the mean fluid speed, R is the streamline radius of curvature, and n is the outward normal to the streamline.

It is beneficial to recast the stability parameter in a form which is easily computed in a general three-dimensional flow. The expression for β can be written as

$$\beta = -(2/R)(V^2/R + 1/2 \partial V^2/\partial n) \quad (31)$$

The pressure gradient normal to streamlines in a steady curved flow is given by

$$\partial p/\partial n = \rho V^2/R \quad (32)$$

so that Eq. (31) becomes

$$\beta = -(2/\rho r) \partial p_t/\partial n \quad (33)$$

in which $p_t = p + \rho V^2/2$ is the incompressible total pressure. Equation (33) reveals that potential flow, for which p_t is constant, is neutrally stable. There are at least two possible ways to compute β . One is to determine the streamline curvature from the pressure gradient, as in Eq. (32), which yields

$$\beta = -2 \frac{\partial p}{\partial n} \frac{\partial p_t}{\partial n} / (\rho^2 V^2) \quad (34)$$

In flows where viscous effects are weak, the total pressure varies slowly along streamlines so that Eq. (34) can be approximated by

$$\beta = -2 \frac{\partial p}{\partial x_i} \frac{\partial p_t}{\partial x_i} / (\rho^2 V^2) \quad (35)$$

Streamline curvature $1/R$ may also be computed from the flow geometry as

$$1/R = \partial \theta / \partial s \quad (36)$$

in which θ is the flow angle and s the distance along a streamline. In three dimensions curvature has both magnitude and orientation and is thus a vector. The curvature vector pointing from the center of curvature outward can be expressed as

$$1/R_i = -U_j/V \partial(U_j/V) / \partial x_j \quad (37)$$

in which V is the velocity magnitude, so that U_j/V is the flow direction. Taking the inner product with $\partial p_t / \partial x_i$ as in Eq. (35) yields

$$\beta = (2/\rho) (U_j/V) \partial(U_j/V) / \partial x_j \partial p_t / \partial x_i \quad (38)$$

Either Eq. (35) or (38) can be used to compute β , and they give similar values except where the assumptions used to derive them are invalid, such as through shocks, in other highly viscous regions, or where the velocity goes to zero. Equation (38) tends to be better behaved in general because it minimizes the problem of the denominator going to zero at stagnation points, and it is used in the present calculations.

The stability parameter is then used to modify the ϵ -equation, by adding the term

$$C_c k \beta \quad (39)$$

to the source term S_ϵ . This choice for the form of the additional source term is not arbitrary, but has been found to perform better than another dimensionally correct form, $C_c \epsilon |\beta|^{1/2} \text{sign}(\beta)$.

Vortex Stretching (Lateral Divergence) - Vortex stretching is often referred to as lateral divergence because it typically involves the lateral stretching ($\partial W / \partial z > 0$) of a two-dimensional shear layer in the x - y plane. By conservation of mass and angular momentum, vortex stretching intensifies vorticity. The effects of vortex stretching on the mean flow are easily treated with the Euler equation. However, its effects on turbulence are complex and not well understood. Obviously, therefore, modeling for the vortex stretching process is not well-developed.

Some first order effects of vortex stretching can be deduced from Eq. (27), the Reynolds-stress production term. For the above example of a typical shear layer, P_{ij} indicates that vortex stretching causes a transfer of turbulence energy from the $w'w'$ component into the $u'u'$ and $v'v'$ components, and that the details of this transfer depend upon the initial turbulence and the strain field. In this shear flow, the increase in $v'v'$ interacts with the mean shear to increase the production of the shear stress. The anisotropic normal stresses interacting with the mean strain cause vortex stretching to transfer energy from the mean flow to the turbulence, especially for strong vortex stretching. Hence, vortex stretching causes the turbulence energy and shear stress to be higher than in a similar flow, but with $\partial W/\partial z = 0$. Consideration of a single vortex subject to stretching leads to similar conclusions.

The effect of vortex stretching should depend significantly on the state of the turbulence, for example, the distribution of the energy among the normal stresses and the structure of the vortices. Wall-bounded flows, round and plane jets, and low- and high-speed free shear layers have very different vortical structures and, hence, should respond differently to vortex stretching.

Modeling for the effects of vortex stretching is in a primitive state, perhaps because of the complexities mentioned above. Pope²¹ suggested vortex stretching as the cause of the "round jet/plane jet" anomaly, in which the round jet spreads less rapidly than the plane jet, but the standard $k-\epsilon$ model predicts the opposite trend. The proposed vortex stretching model was an additional source term in the ϵ -equation

$$C_{vs} G \chi k^2 / \epsilon \quad (40)$$

in which the vortex stretching is given by,

$$\chi = \Omega_i \Omega_j S_{ij} \quad (41)$$

the vorticity is

$$\Omega_i = \epsilon_{ijk} \partial U_k / \partial x_j \quad (42)$$

with ϵ_{ijk} being the alternating third rank tensor, and the strain rate tensor is given by

$$S_{ij} = (\partial U_i / \partial x_j + \partial U_j / \partial x_i) / 2 \quad (43)$$

In Pope's model the function $G = 1$. The model coefficient was optimized to be $C_{vs} = 0.79$, and the model then gave the correct spreading rate for the round and plane jets. In a flow in which vortex stretching occurs, Eq. (40) increases the dissipation which reduces the eddy viscosity.

Unfortunately, this model produces the wrong trend in a radial wall jet,²² which is a flow of major interest for impinging jet predictions, and in the radial free jet. The shear stress in these two flows is considerably higher than in their two-dimensional counterparts, whereas the Pope modification reduces the modeled shear stress.

To make the k - ϵ model sensitive to the vortex stretching which is so pervasive in impinging jet flows, a modification of the form of Eq. (40) must be used. Note that the sign of C_{vs} required for impinging jets is *opposite* of that used by Pope. A further difficulty must also be corrected. Apparently because of their differing vortical structure, the free and wall-bounded jets require slightly different modeling. An *ad hoc* remedy is to make G a function of wall proximity,

$$G(L/y) = 1. + C_{vs2} L / y \quad (44)$$

in which $L = C_{\mu}^{3/4} k^{3/2} / \epsilon$ is the turbulent mixing length and y is the distance from the wall. To ensure the model is robust, L is limited to $L \leq y$. This form of the model makes it possible to match the growth rates of free and wall-bounded radial jets. A less empirical wall treatment would require knowledge of the turbulence structure which is not readily available from the k - ϵ model.

The full source term for the ϵ -equation, including curvature and vortex stretching effects, can be written as

$$S_{\epsilon} = C_{\epsilon 1} \rho \frac{\epsilon}{k} P_k - C_{\epsilon 2} \frac{\rho \epsilon^2}{k} + C_c k \beta + C_{vs} G(L/y) \chi \frac{k^2}{\epsilon} \quad (45)$$

Disadvantages of Vortex Stretching Model - Despite the need for a model of vortex stretching effects on turbulence, the model presented above can cause difficulties in calculations of some flows. As noted previously, the physics of vortex stretching is complex and poorly understood, and only a few efforts have specifically addressed the issue of modeling for this phenomenon.

For radial jets, C_{vs} must have the opposite sign of that used by Pope.²¹ However, this value of C_{vs} exacerbates the problem which Pope addressed: the k - ϵ model's error in a round jet. The wall-proximity function $F(L/y)$ causes the vortex stretching effects to be relatively small away from the wall, so that this extra error in the round jet remote from walls is also small. It is now well-known that coherent structures dominate the momentum transport by turbulence, and that these structures differ from flow to flow. For example, the dominant structures in low-speed plane shear layers consist of spanwise vortices, while fully developed round jets contain helical vortices. It has been proposed²³ that helical or swept vortices are less efficient than spanwise ones at generating mixing. Thus, vortex orientation may be the cause of the round jet-plane jet anomaly, rather than vortex stretching. The k - ϵ model has no "knowledge" of vortical structure and cannot model the effects of structural changes. There remains a fundamental and practical issue concerning the k - ϵ model's accuracy for round jets.

A second difficulty is related to the mathematically ill-posed nature of the k - ϵ model. Ratios of k and ϵ which appear many places in this model, and, in laminar flow, these ratios are singular. Physically these ratios must be reasonably well-behaved. However, numerical solutions of the turbulence model equations do not provide any such guarantees, and many codes which use the k - ϵ model employ artificial limits which insure that $k, \epsilon > 0$. These limits do not impart physically correct behavior to the model; they merely prevent the modeled solution from diverging, under most circumstances. The presence of ϵ in the

denominator of Eq. (40) gives the vortex stretching term the ability to exhibit ill-conditioned behavior. Vortex stretching causes ϵ to decrease to provide a higher shear stress, but this change also increases the magnitude of the vortex stretching term. This nonlinear decrease of ϵ , and, hence, increase of μ_v , in the presence of vortex stretching may be somewhat physical; analysis of the production terms in the Reynolds-stress transport equations indicates that vortex stretching is a nonlinear process. However, the limits to stress amplification which govern physical turbulence are not present in the $k-\epsilon$ model.

One of the conclusions of this work is that, while vortex stretching is a critical process which must be included in a model of turbulence, a deeper understanding of the physical processes and a mathematically well-posed model should be pursued in future basic research in this area.

Model Nomenclature - For brevity and clarity, the following abbreviations will be used in discussing the results given with possible forms of the $k-\epsilon$ model.

- STD standard model defined by Eqs. (24-29),
- C with curvature modification, Eqs. (38, 39),
- VS with vortex stretching modification, Eqs. (40-44),
- CVS with curvature and vortex stretching modifications.

For illustrative purposes, the different possible combinations of model modifications will be used to compute flows. However, the CVS model is believed to be the most accurate of those considered here, and it should be used for all impinging jets flow calculations.

Model Calibration - The new model coefficients introduced with the curvature and vortex stretching modifications are determined by numerical optimization for simple flows that are specific to the phenomena of streamline curvature and vortex stretching.

The three flows used in the model calibration are self-similar in the streamwise direction: a wall jet over a convex logarithmic spiral, a radial wall jet, and a radial free jet. Consensus values for the growth rate and maximum shear stress in wall jets were obtained from a review by Launder and Rodi,²⁴ while the free jet data is from Witze and Dwyer.²⁵ A computer program for self-similar flows was used so that very good numerical resolution was possible. The computed results were grid-independent. The standard model coefficients C_μ , $C_{1\epsilon}$, $C_{2\epsilon}$, σ_k , σ_ϵ , and Pr_t are unchanged from the values used by many modelers.¹⁵ Pr_t is the turbulent Prandtl number. The model coefficients are given in Table 2.

Table 2. Model Coefficients.

C_μ	$C_{\epsilon 1}$	$C_{\epsilon 2}$	C_c	C_{vs}	C_{vs2}	σ_k	σ_ϵ	Pr_t
0.09	1.44	1.92	0.2	-0.15	4.0	1.0	1.3	0.9

C_c is similar to the values selected by Launder et al¹⁸ and Rodi and Scheuerer²⁰ for several different flows, while C_{vs} is very different from previously used values.^{21,26}

A comparison of experimental data and computed model results for the growth rate of the curved wall jet is given in Figure 21. At zero curvature the growth rate $\partial y_{1/2} / \partial x = 0.073$,

in which $y_{1/2}$ is the half-velocity thickness. The $k-\epsilon$ model gives a growth rate of $\partial y_{1/2} / \partial x = 0.09$, which is 23% high and which is typical for this model. C_c was selected to match the change of growth rate with respect to curvature, $\partial(\partial y_{1/2} / \partial x) / \partial (y_{1/2} / R)$, and, hence, it is not surprising that the CVS model performs well over the full range of streamline curvature. Also included for comparison are results from the STD model, which gives only about 25% of the increase in growth rate due to curvature. The slight increase in the growth rate is due to the additional shear associated with the streamline curvature.

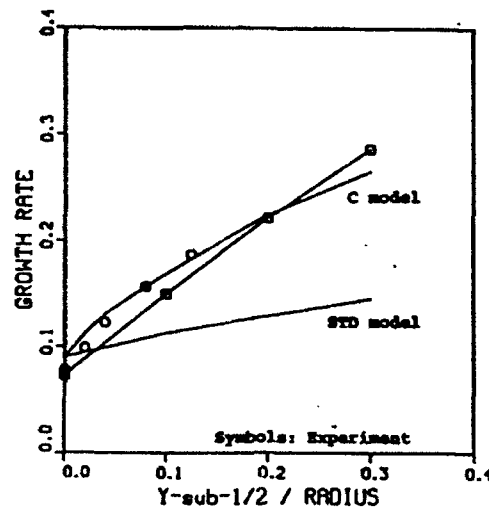


Figure 21. Growth rates of self-preserving wall jet on a logarithmic spiral, experiment and calculations with the STD and C models.

The measured and predicted growth rates of the free and wall jets in planar and radial configurations are given in Table 3. The standard model underpredicts the growth rate of the radial jets by a substantial amount. C_{vs} and C_{vs2} were selected to reproduce the change in growth rate due to streamline curvature, and, because of the model's error for the plane wall jet, the CVS model does exhibit some error for these radial flows.

Table 3. Calibration Flows for Vortex Stretching Model

		Growth Rate, $dy_{1/2} / dx$		
		Exp.	STD Model	CVS Model
Plane:	Free Jet	0.10 - 0.11	0.11	—
	Wall Jet	0.073	0.09	—
Radial:	Free Jet	0.10	0.087	0.11
	Wall Jet	0.09	0.54	0.10

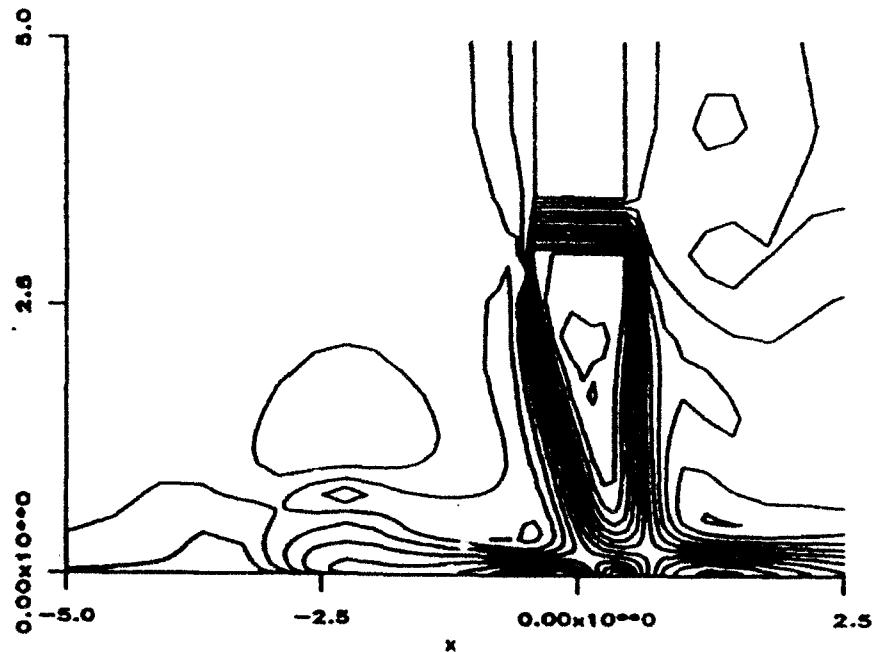
6. REYNOLDS-AVERAGED IMPINGING JET CALCULATIONS

Results are presented for Reynolds-averaged calculations of three impinging jets in crossflow. The experiments of these flows were conducted in small wind tunnels. In the calculations, the tunnel geometry has been represented as faithfully as possible. The tunnel side walls are included in all calculations, and the wind tunnel top wall is included in Cases I and II. For Case III, the tunnel section was rather tall, roughly ten times the height of the ground vortex. A shorter computational domain was used with free inflow-outflow boundary conditions imposed on the top of the domain to reduce the computational cost. The pipe which supplies the jet has been approximated with interior boundary conditions in all cases. While the experiments are at incompressible speeds, the calculations were run at intermediate jet Mach numbers, typically $M_j = 0.5$, to maintain computational efficiency with the compressible algorithm; compressibility effects in the computed results are negligible.

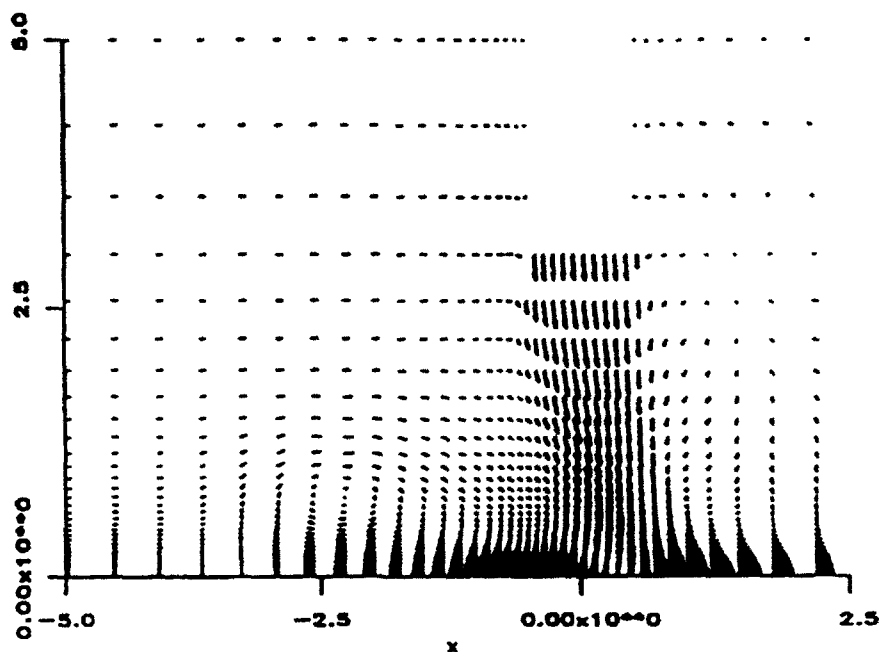
Case I: Normal Jet, $H/D = 3$, $V_j/V_\infty = 5$

This case is of a jet with a nearly uniform velocity issuing from a nozzle normal to the plate. The crossflow causes significant deflection before the jet strikes the ground. This flow has been studied experimentally by Cimbalá et al,¹² using laser velocimetry, surface pressures and flow visualization.

The velocity magnitude contours and velocity vectors from the solution computed with the CVS model are given in Figure 22. The jet flows downward from $x/D_j = 0$ and $y/D_j = 3$. The cross flow from the left in the figure causes the ground vortex to form on the left of the impingement point. The general features of the flow are easily identified in this figure.



(a) Velocity magnitude



(b) Velocity vectors

Figure 22. Velocity magnitude contours and velocity vectors on the center plane, computed with the CVS model, for Case I.

Surface centerline pressure coefficients from experiment and calculations are given in Figure 23. The high pressure corresponds to the impingement point, while the low pressure upstream of the impingement point indicates the position of the ground vortex. For this flow, the STD model predicts the ground vortex to be too far upstream of the experimental location by about 50%. (Upstream is with respect to the crossflow.) This type of error, including direction and magnitude, has also been obtained by other researchers, as noted in the Introduction. The C model predicts the ground vortex to be even further upstream of the experimental location, which increases the error relative to the STD model. The VS model predicts the ground vortex to be in virtually the correct location, while the CVS model places the ground vortex upstream of the experimental location by about 13%.

A comparison of measured velocity vectors and those computed with the CVS model in the ground vortex is given in Figure 24. As in Figure 23, the computed ground vortex location is slightly upstream of the experimental location, which is consistent with the surface static pressures.

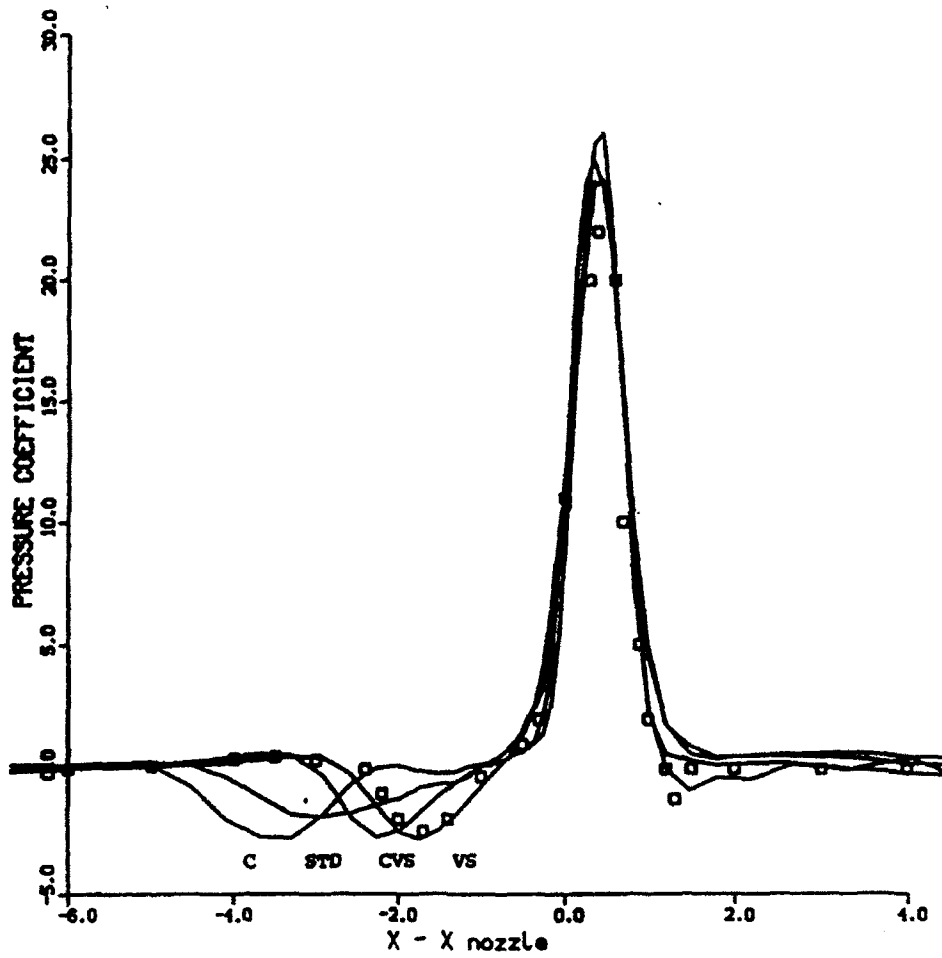
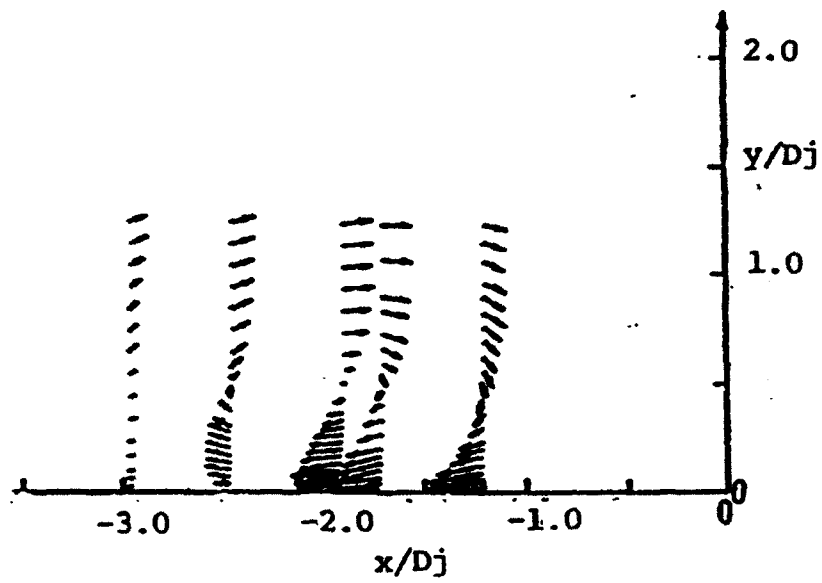
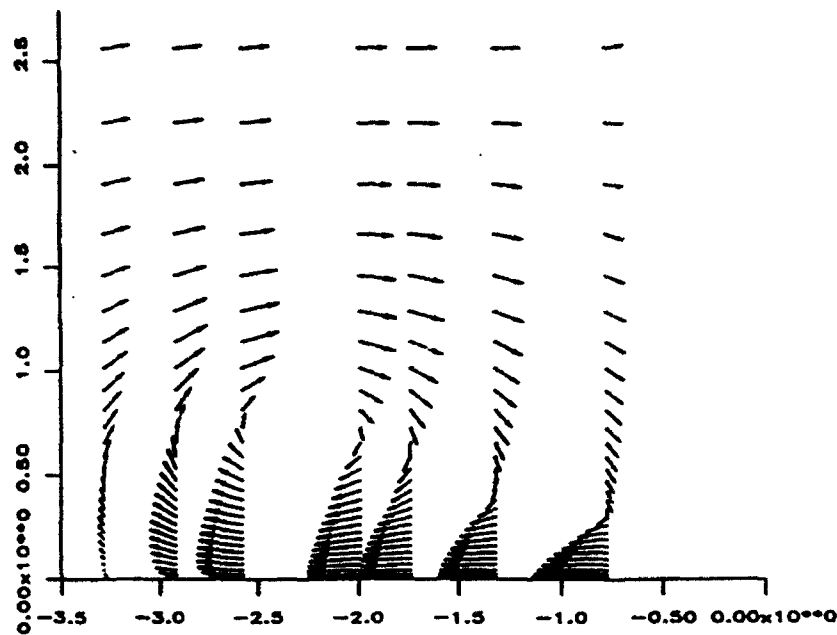


Figure 23. Surface centerline static pressure distribution for Case I.



(a) Measured velocity

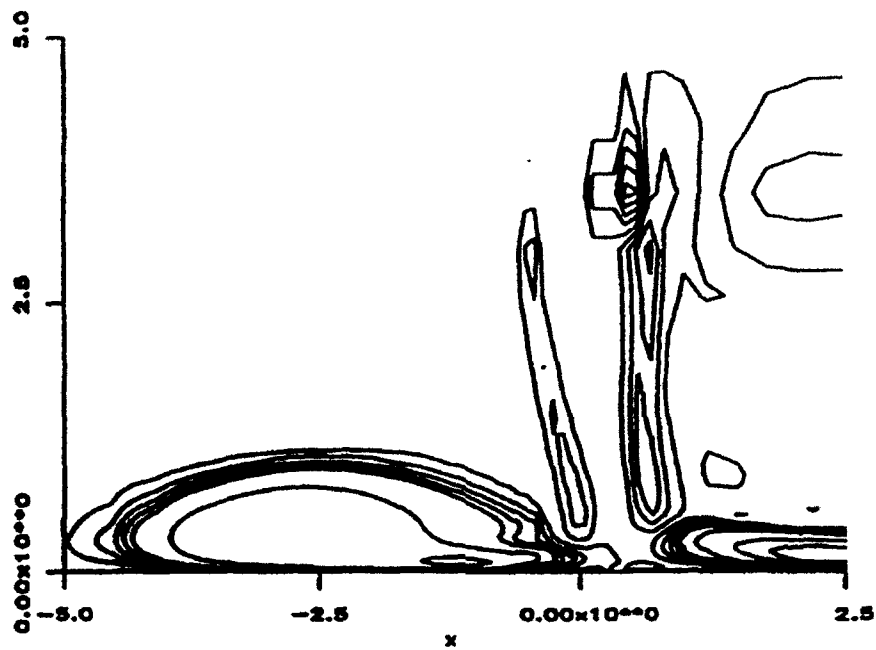


(b) Measured velocities

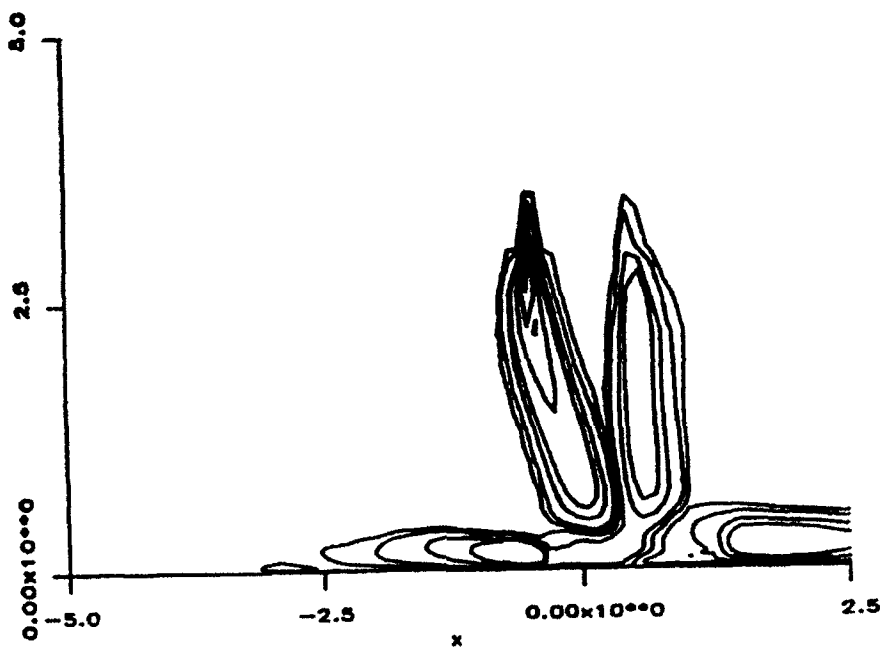
Figure 24. Comparison of center plane mean velocity vectors for Case I computed with the CVS Model and measured by Cimbala et al.²⁹

The surface pressure measurements with the VS model are very close to the experimental data, but this model modification alone cannot be truly correct. Despite the small degradation in accuracy, the curvature modification must be included in calculations of this flow. The curvature modification is required to compute accurately the shear stresses in the impingement zone of a normally impinging jet,²⁷ the curved-wall jet, and other curved flows. This result also indicates that the apparent marginal accuracy of the STD model is, in fact, due to luck, because the errors incurred by not accurately predicting curvature and vortex stretching effects are of opposite sign.

The significance of the CVS model modifications to the computed turbulence levels can be seen in the predicted centerplane shear stress, given in Figure 25. The STD model predicts the shear stress in the vortex core ($x/D_j = -2.5$, $y/D_j = 0.5$) to be very nearly the maximum in the domain, exceeding the stress in the free jet by more than a factor of 5. Laser velocimetry measurements by Barata²⁸ of a normal impinging jet at $H/D = 5$ and $V_j/V_\infty = 30$ indicate that the shear stress in the vortex is roughly an order of magnitude less than the peak values in the free jet. In contrast, the CVS model predicts the shear stress to be small in the ground vortex and relatively larger in the free jet. Hence, the CVS model displays results which are consistent with the trends seen in impinging jet experiments.



(a) STD model



(b) CVS model

Figure 25. Comparisons of $\overline{u'v'}$ the center plane of Case I computed with the STD and CVS models.

One disturbing characteristic of the CVS prediction is that the maximum predicted shear stress occurs just downstream of the jet exit on the upstream side of the jet. Experiments indicate the shear stress is small near the nozzle and grows in the downstream direction. This region of maximum shear stress experiences vortex stretching, because $\partial W/\partial z$ is large as the crossflow is deflected around the normal jet. Furthermore, the freestream has low values of k and ϵ . This combination of vortex stretching and nearly laminar flow can cause the model to display ill-conditioned behavior, as noted previously. The high shear stress near the nozzle exit is probably due to this problem of ill-conditioning. This shortcoming is, in some respects, an inherent disadvantage of all multi-equation models that involve ratios of turbulence variables which become singular in laminar flow.

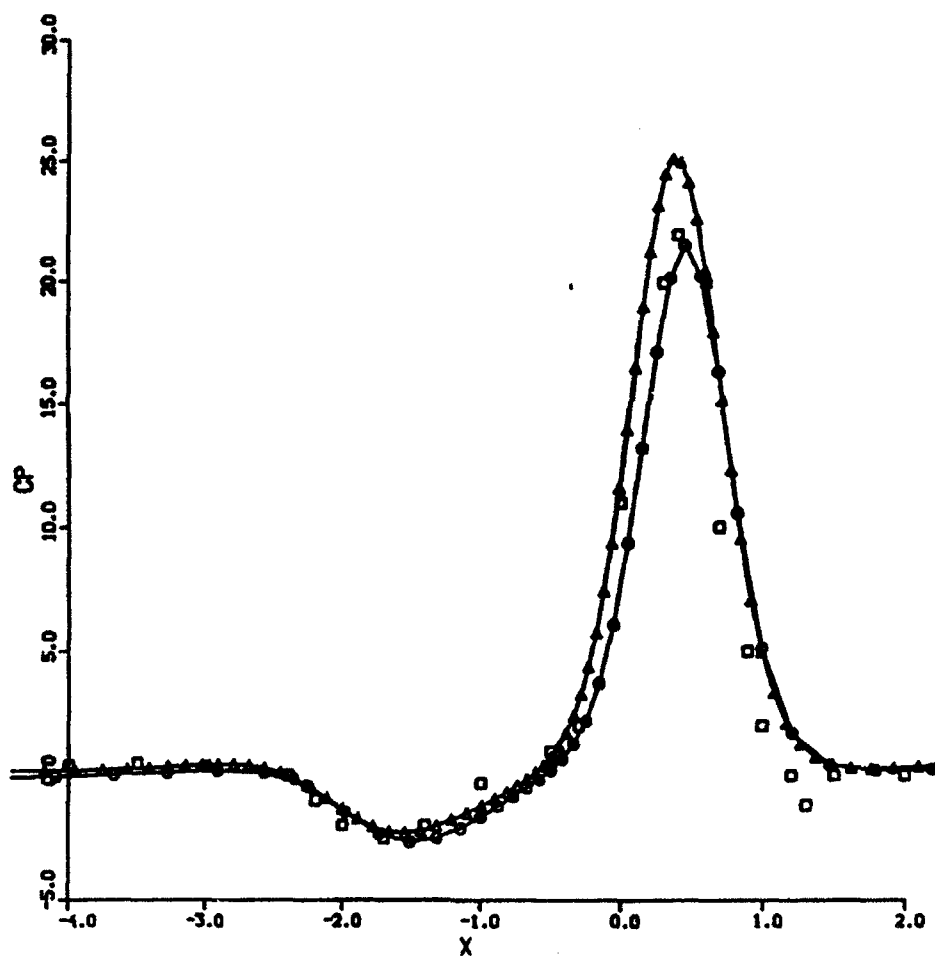


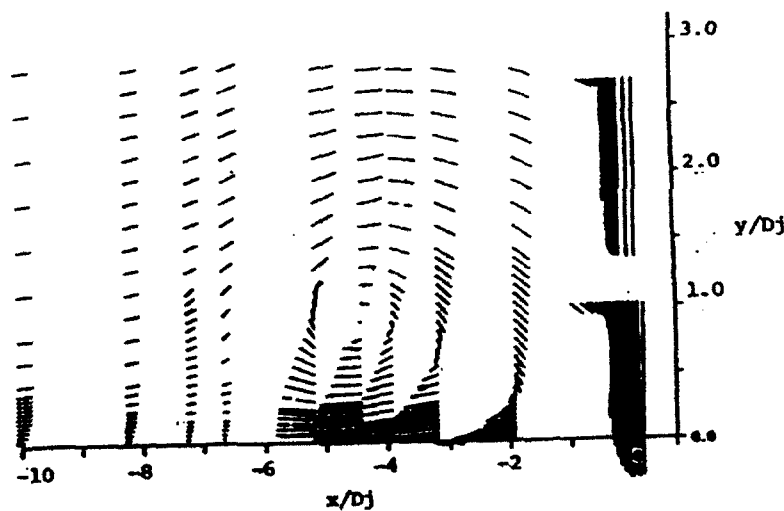
Figure 26. Surface centerline pressure distributions computed in grid refinement study.

Grid Dependence - The grid dependence was evaluated for this case by comparing calculations on two different grids, one which contained $50 \times 35 \times 28$ points in the x - y - and

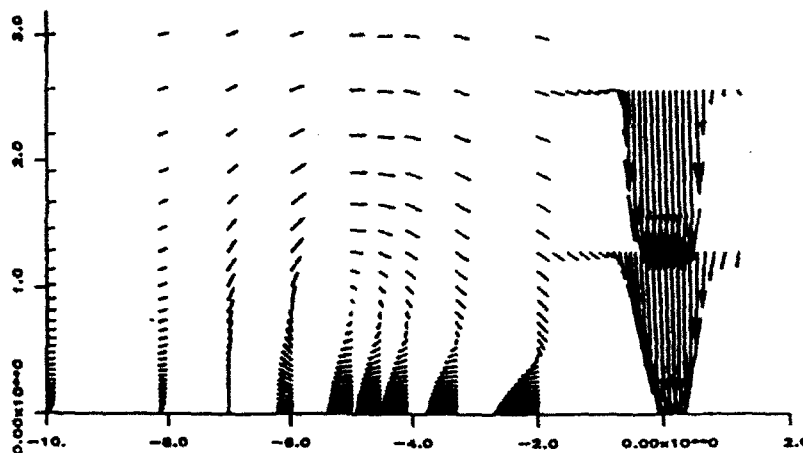
z-directions and was typical of the grids used in this study, and one which contained $94 \times 46 \times 44$ grid points. In the finer grid, the grid spacing was approximately half of that in the regular grid, in the free jet, the impingement region, and ground vortex region. This should reduce the truncation by a factor of roughly 16 because most error is due to the inviscid terms which are discretized with fourth order accuracy. The calculations were performed with the VS model, although the specific model is largely irrelevant in a grid refinement study. Figure 26 gives the centerline surface pressure distribution under the impingement point and ground vortex. The biggest difference is seen in the peak pressure, with the fine-grid solution giving a higher pressure. This result is consistent with the reduced "numerical diffusion" in the fine-grid solution of the free jet. The position of the ground vortex, associated with the low-pressure region, is very similar for the calculations on both grids, and, consistent with the reduced losses due to numerical diffusion, the ground vortex in the fine-grid calculation is forward of that on the regular grid. However, the dependence of the computed vortex location upon the grid is significantly less than the dependence upon the turbulence model, and turbulence modeling can be addressed without significant concern regarding truncation errors.

Case II: Normal Jet, $H/D = 3$, $V_j/V_\infty = 10$

This case was also measured by Cimbalá et al,²⁹ and the jet configuration is similar to Case I, except for the velocity ratio. A significant part of the experimental study focused on vortex unsteadiness, and the core vortex height fluctuates $\pm 30\%$ in this flow. Figure 27 gives a comparison of the time-averaged velocity vectors in the impinging jet and ground vortex region computed with the CVS model and the experimental data. The location of the ground vortex core is measured to be at $x/D_j = 4.5$ and $y/D_j = 0.9$. The computed location is at $x/D_j = 5.25$ and $y/D_j = 1$. The computed vortex core location is about 17% too far upstream, compared to the experimental location.



(a) Measured velocities



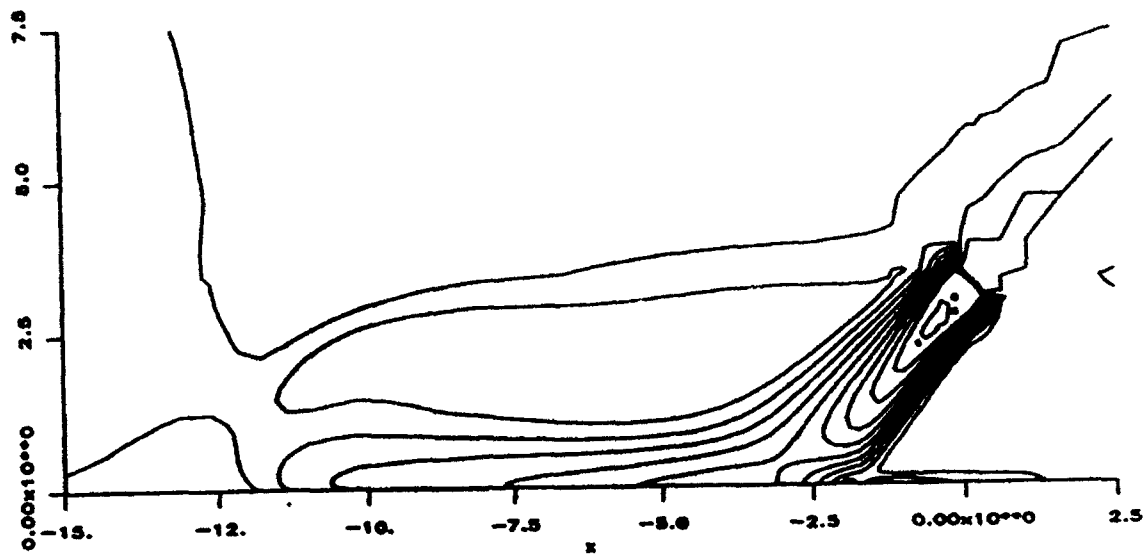
(b) Predicted velocities

Figure 27. Comparison of center plane mean velocity vectors for Case II computed with the CVS model and measured by Cimbala et al.²⁹

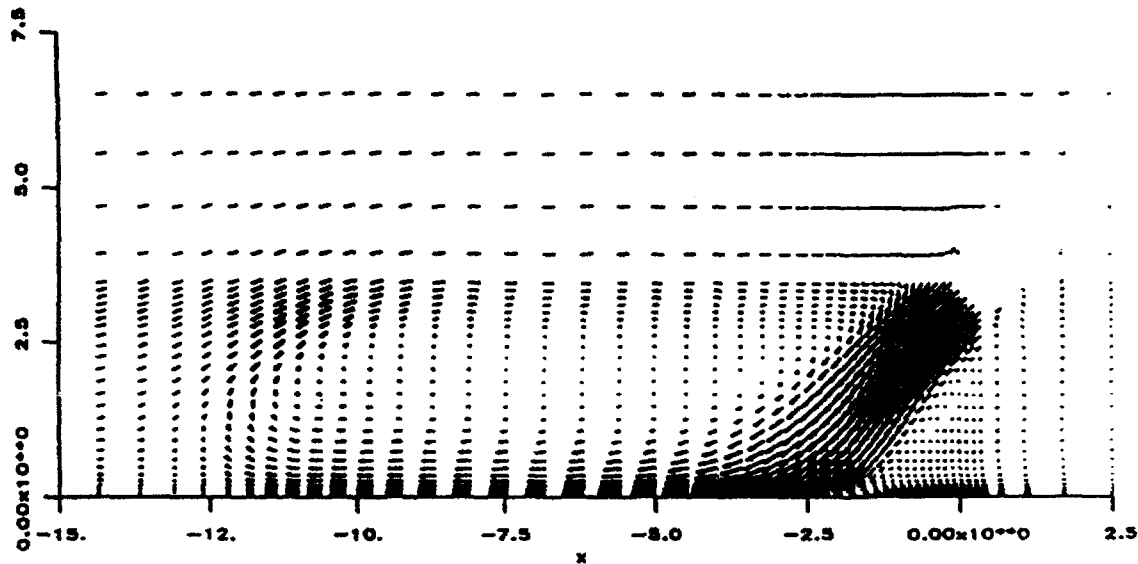
The most significant other difference is that the shear layer on the free jet is thicker in the calculation than in the experiment. There are between 5 and 9 grid points across the shear layer at the plotted locations, which should be sufficient for good numerical resolution of the mean flow with the present differencing scheme. Hence, the excessive spreading is probably caused by the turbulence model. As noted previously, the standard $k-\epsilon$ model overpredicts the spreading rate of the round jet, and the vortex stretching modification exacerbates this problem. While some of the physics of this issue are understood, no suitable model correction has yet been proposed.

Case III: Inclined Impinging Jet

The final calculation presented is of the primary experimental case, which is an impinging jet inclined 45° toward the crossflow. The jet is close to fully developed turbulent pipe flow with a jet centerline velocity ratio $U_{j,cl}/U_\infty = 5.27$, and $H/D_j = 3.1$. The wind tunnel cross section is 76.2 cm (30 in) square and the jet exit diameter $D_j = 2.87$ cm. The nozzle exit centerline speed is approximately 26 m/s. The developed turbulent jet was used in this case because an important application of inclined jets is for thrust reversing; the reversing process on jet engines tends to generate a turbulent jet.

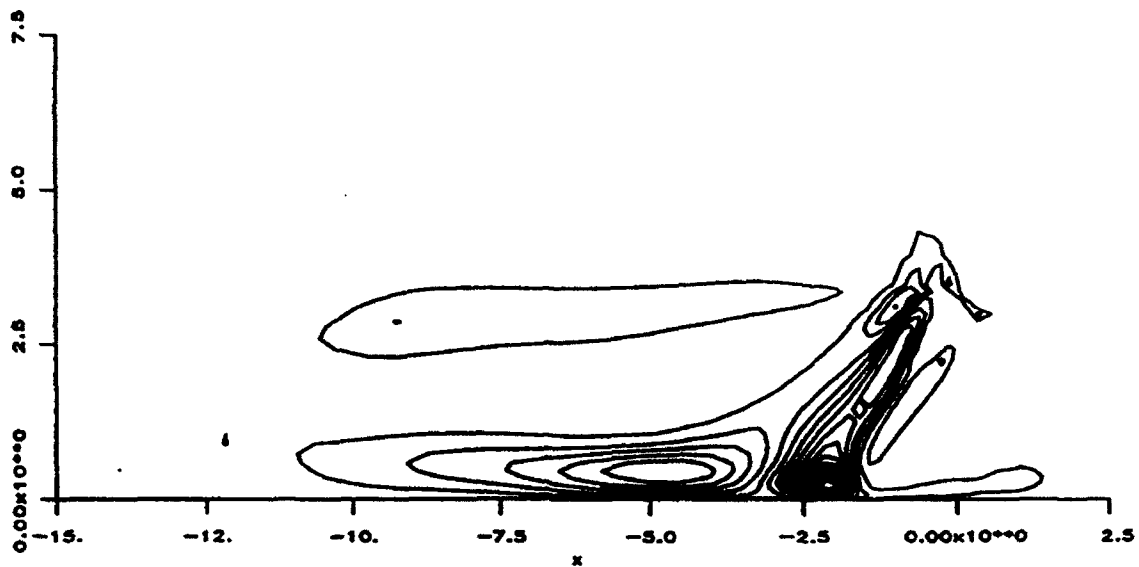


(a) Velocity magnitude



(b) Velocity vectors

Figure 28. Contours of velocity magnitude, velocity vectors, and contours of the shear stress $u'v'$ on the center plane for Case III predicted with the CVS model.



(c) Shear stress

Figure 28. Contours of velocity magnitude, velocity vectors, and contours of the shear stress $\overline{u'v'}$ on the center plane for Case III predicted with the CVS model.

Velocity magnitude contours, velocity vectors, and contours of the shear stress $\overline{u'v'}$ predicted with the CVS model are given in Figure 28. In the velocity magnitude contours and velocity vectors, the primary features of the flow can be seen. The inclined jet has no potential core, and the velocity magnitude decays significantly before reaching the ground. The majority of the jet flow goes forward after the interaction with the ground, and the forward extent of the ground vortex, defined by the separation line between the crossflow and the ground vortex, is about $x/D_j \approx -13$. The contour plot of $\overline{u'v'}$ must be interpreted correctly because the impinging jet is at -45° to the principal grid axis. The "effective shear stress" which transports momentum away from the jet does not appear as $\overline{u'v'}$, but is shared by $\overline{u'u'}$, $\overline{v'v'}$, and $\overline{u'v'}$, according to rules of tensor rotation. The areas of maximum $\overline{u'v'}$ are the windward shear layer of the impinging jet, a region near the downstream edge of the impingement zone, and in the wall jet running forward from the impingement point. As in Case I, there is negligible shear stress in the vortex core. This plot also reveals a region of shear stress in the ground vortex, but above the core.

The accuracy of the model predictions is best assessed in a plot of the centerline surface pressure coefficient, given in Fig. 29. For this flow, the STD model underpredicts the forward extent of the ground vortex, defined by the location of minimum pressure, by roughly 30%, while the CVS model predicts the position of the ground vortex core to be roughly 18% upstream of the measured value. The VS model causes the ground vortex to move backward slightly from the location predicted with the STD model, further degrading the accuracy. This result clearly indicates that the apparent accuracy of the VS model in Case I is a result of luck, rather than fundamentally correct turbulence modeling.

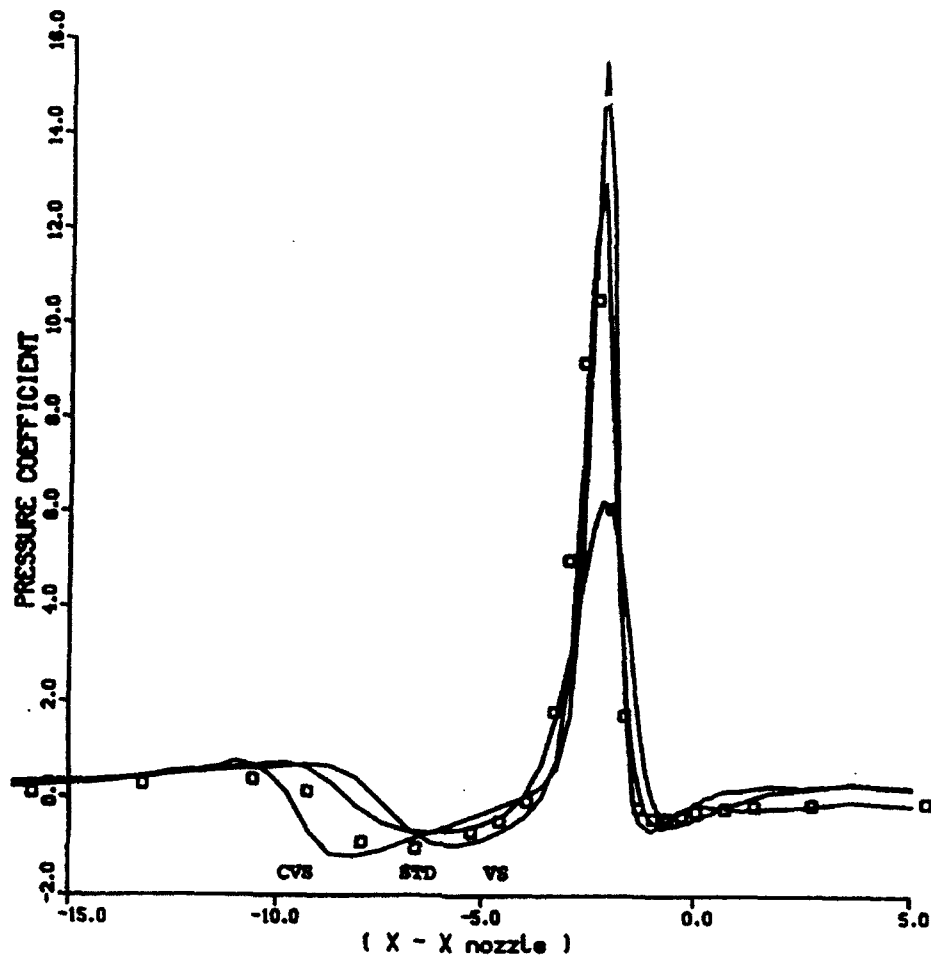


Figure 29. Surface centerline static pressures for Case III.

There are significant differences in the predicted maximum wall pressures under the impingement region, and the specific causes of the differences are not known. Several factors affect this pressure. The vortex stretching model may overpredict the turbulent stresses in the round jet above the impingement point, which affects the jet deceleration and deflection by the crossflow. The maximum static wall pressure is not the maximum jet stagnation pressure, because the stagnation streamline does not correspond to the jet centerline in an inclined jet. Hence, differences in the predicted turbulence may generate significant differences in the maximum surface pressure, and the relationship between the pressure and predicted turbulence is not obvious.

Interpretation of Reynolds-Averaged Results

The above results provide a self-consistent description of the deficiencies of the standard $k-\epsilon$ model, and of the improvements in accuracy given by modifications to the standard model to account for effects of curvature and vortex stretching.

The STD model predicted the ground vortex to be 50% forward of its measured location in Case I and 30% downstream in Case III. This 80% discrepancy in the predicted relative ground vortex locations indicates that powerful turbulence-modifying phenomena occur in the impingement region, which depend significantly upon the angle of the jet. The VS modification produced changes in Cases I and III that were of the same sign; the same was true for the C modification. However, the CVS modification causes the ground vortex to move downstream in Case I and upstream in Case III, which indicates that the predicted relative effects on turbulence of vortex stretching and curvature are different in the two cases.

The wall jet upstream of the impingement point spreads out more rapidly in the normal impinging jet than in the inclined impinging jet. Hence, $\partial W / \partial z$, appropriately normalized, is larger for the normal impinging jet, and vortex stretching effects in the wall jet are stronger in Case I than in Case III. Differences in streamline curvature in Cases I and III are appreciable in the impingement region, and should produce differences in the modeled (and physical) turbulence there. However, the region of strong curvature in the impingement zone is small relative to the extent of the radial-like wall jet. Furthermore, turbulence in the vortex core is suppressed, and the predicted turbulent shear stress in the vortex cores approaches zero in Cases I and III. There is no comparable limit to turbulence amplification in the wall jet. Hence, the significant differences seen in the accuracy of the STD model for the different impinging jet flows is apparently due to that model's inability to predict the effects of vortex stretching upstream of the impingement point.

The CVS model gave a significant improvement over the STD model in Cases I and II, and consistently predicted the ground vortex location in all three cases considered here to be 13% - 18% upstream of the measured location. Hence, the errors in solutions predicted by the CVS model are one-half to one-third of the errors given by the STD model, and they are consistent across the cases examined.

The errors given by the CVS model are not, however, small enough to be disregarded, and some means of reducing these errors is desired. In the use of most turbulence models, the model coefficients can be adjusted to tune the model predictions for a certain class of flows. The calculations presented above were obtained with model coefficients tuned for benchmark flows which were totally distinct from impinging jet flows. It is legitimate to change these coefficients, provided the coefficients can be held constant for the entire class of flows of interest. An attempt was made to optimize the coefficients C_{vs} and C_{vs2} for flows including the wall jet and impinging jet flows. The coefficients were changed to increase effects of near-wall vortex stretching and reduce its effects in regions far from a wall. One objective of this test was to reduce the very high stresses seen near the nozzle exit in Case I. However, the results of this test were negative; it was not possible to improve the predicted ground vortex location with a pair of coefficients that would also predict the radial wall jet accurately. The inability to obtain improved accuracy in a range of flows by adjusting model coefficients suggests that the underlying physical mechanisms must be represented more accurately in the turbulence model.

7. CONCLUSION

The present study addresses the accuracy of the $k-\epsilon$ turbulence model for inclined impinging jet flows typical of thrust reverser application in close ground proximity, particularly those which generate a complex recirculating flow field.

The thesis of the present report is that streamline curvature and vortex stretching are the two most significant influences on turbulence in these flows which are not treated adequately in the "standard" $k-\epsilon$ model. Streamline curvature has been recognized as a critical turbulence modifier for many years. The significance of vortex stretching in impinging jet flows was recognized in the large eddy simulations performed in this study. As vortical structures flow outward from the impingement point in a radial-like wall jet, the structures contract and intensify due to conservation laws for mass and angular momentum. Instantaneous and time-averaged results from the large eddy simulations reveal that the shear stress is amplified by the vortex stretching process.

Modifications which account for curvature and vortex stretching were added to the standard $k-\epsilon$ model, and the new coefficients in the resulting modified model, denoted the CVS model, were determined via numerical optimization for benchmark jet flows unrelated to the impinging jet flows of primary concern.

In the three cases considered, two impinging jets issuing from a nozzle normal to the ground plane and one issuing from a nozzle inclined 45° into the crossflow, the CVS model consistently improved the accuracy for the computed location of the ground vortex. Errors in the computed vortex location, relative to the distance between the impingement point and the ground vortex core, were as large as 50% in calculations with the standard $k-\epsilon$ model and could be of either sign (overprediction or underprediction of the ground vortex's forward extent). The CVS model reduced these errors to the range of 13%-18%, and it consistently overpredicted the upstream penetration of the ground vortex.

Recommended Future Work

There are a few significant shortcomings in the turbulence model at this time. The first is a flaw in the STD model: it cannot accurately predict the "simplest" elements of thrust reverser flow fields. It does not properly predict a planar wall jet on a flat surface or a round jet if the model coefficients have been adjusted, as is normally done, to predict the widest range of generic turbulent flows. The standard $k-\epsilon$ model simply does not have the capacity to respond to the physically relevant parameters such as wall proximity, in the wall jet, or the change of dominant vortical structure, as in the round jet. These errors are of the order of 10% to 20%, which is large enough to make a significant contribution to the total error, or mask other errors, in the calculation of a complex impinging jet flow.

An additional problem is that the $k-\epsilon$ model, as with many multi-equation models, is singular in laminar flow. Although the ratio k/ϵ may be well-defined physically, even small truncation errors can generate non-physical values of k and ϵ which will cause the modeled solution to behave erratically. If the objective of developing good turbulence models for complex flows is to be achieved, these models must be well-posed for integration by numerical schemes of finite accuracy.

Modeling of the vortex stretching process may also benefit from further work. The present study has identified vortex stretching as a critical physical aspect of impinging jet flows and has employed a relatively simple model for this process. However, it has not been possible to obtain a good understanding of the physics of vortex stretching, nor has it been possible to develop a very good model of this physics.

It is not difficult to make general recommendations for research work that will address the above problems: employ turbulence simulations and experiments symbiotically to identify the dominant turbulent physics, discriminate between that which can be modeled simply and that which is complex, and construct a mathematically well-posed model that resolves that dominant, complex physics. Unfortunately, decades of research have not yet achieved these goals.

Specific recommendations to improve $k-\epsilon$ modeling for thrust reverser flows are somewhat more difficult to put forth. Clearly, the effects of vortex stretching on turbulence should be the topic of a basic research effort. The roles of the inherent vortex structure, the modification of that structure by stretching, and the subsequent effect on turbulent mixing must be known. These results should give a strong indication of the correct direction for future modeling work. It is believed that the $k-\epsilon$ model carries too little information about turbulence to permit it to make good predictions of the wide range of flow phenomena which occur in thrust reverser flow fields. This does not imply that the next conventional step in the turbulence modeling hierarchy, the Reynolds-stress transport model (RSTM), is the appropriate model to pursue. The RSTM's accuracy for the plane wall jet, for example, is worse than that of the standard $k-\epsilon$ model. Instead, it is believed that a model which contains information about the dominant vortical structure will be required to achieve a significant improvement over existing models.

REFERENCES

1. Joshi, P. B. and Compton, M. K., "Approach and Landing Thrust Reverser Testing in Ground Effect," AIAA-85-3075.
2. Capone, F. J. and Mason, M. L., "Interference Effects of Thrust Reversing on Horizontal Tail Effectiveness of a Twin Engine Fighter Aircraft at Mach Numbers from 0.15 to 0.90," NASA TP-2350, 1984.
3. Blake, W. B., "F-15 SMTD Low Speed Jet Effects Wind Tunnel Test Results," NASA CP-10008, 1987, pp. 91-120.
4. Kuhn, R. E., "V/STOL and STOL Ground Effects and Testing Techniques," NASA CP-2462, pp. 1-145.
5. Penrose, C. J., "The Scaling of Model Test Results to Predict Intake Hot Gas Reingestion for STOVL Aircraft with Augmented Vected Thrust Engines," NASA CP-2462, 1987, pp. 309-339.
6. Johns, A. L. and Biesiandy, T. J., "Hot Gas Ingestion: From Model Results to Full Scale Testing," NASA CP-2462, pp. 341-361.
7. Huang, G. P., "The Computation of Elliptic Turbulent Flows with Second-Moment-Closure Models," Ph. D. Thesis, Univ. Manchester Inst. of Sci. and Tech., 1986.
8. Kuhn, R. E., Del Frate, J. H., and Eshleman, J. E., "Ground Vortex Flow Field Investigation," NASA CP-10008, 1987, pp. 61-90.
9. Patel, V. C., "Calibration of the Preston Tube and Limitations on its Use in Pressure Gradients," J. Fluid Mech. 1965, vol 23, part 1, pp. 185-208.
10. Childs, R. E., Rodman, L. C., and Nixon, D., "Methods for Computational Aeroacoustics," Nielsen Engineering & Research NEAR TR 452, Aug. 1992.
11. Thompson, K. W., "Time Dependent Boundary Conditions for Hyperbolic Systems," J. Computational Physics, Vol. 68, No. 1, January 1987, pp. 1-24.
12. Cimbala, J. M., Stinebring, D. R., Treaster, A. L., Billet, M. L., and Walters, M. M., "Experimental Investigation of a Jet Impinging on a Ground Plane in a Crossflow," J. Aircraft, Vol. 25, No. 10, Oct 1988, pp. 923-931.
13. Childs, R. E., Bower, W. W., Chmielewski, G. E., and Howe, M. S., "Jet Noise Predictions from Unsteady Navier-Stokes Simulations," AIAA-91-0493.
14. Mavripiis, D. J. and Jameson, A., "Multigrid Solutions of the Navier-Stokes Equations on Triangular Meshes," AIAA J., Vol. 28, No. 8, 1990, pp. 1415-1425.
15. Kline, S. J. et al., eds., The 1980-81 AFOSR-HTTM-Stanford Conference on Complex Turbulent Flows, Stanford University, 1981.
16. Rayleigh, Lord, "On the Dynamics of Revolving Fluids," Proc. Royal Society, Vol. 93, 1916, p. 193.
17. Bradshaw, P., "Effects of Streamline Curvature on Turbulent Flow," AGARDograph No. 169, 1973.
18. Launder, B. E., Priddin, C. H., and Sharma, B. I., "The Calculation of Turbulent Boundary Layers on Spinning and Curved Surfaces," J. Fluids Engrg., Mar. 1977, pp. 231-239.
19. Leschziner, M. A. and Rodi, W., "Computation of Strongly Swirling Axisymmetric Free Jets," AIAA J., Vol. 22, No. 12, 1984, pp. 1742-1747.
20. Rodi, W. and Scheuerer, G., "Calculation of Curved Shear Layers with Two-Equation Turbulence models," Phys. Fluids, Vol. 26, No. 6, 1983, pp. 1422-1436.
21. Pope, S. B., "An Explanation of the Turbulent Round Jet/Plane Jet Anomaly," AIAA J., Vol. 16, No. 3, pp. 279-281.

22. Rubel, A., "On the Vortex Stretching Modification of the $k-\epsilon$ Turbulence Model: Radial Jets," AIAA J., Vol. 23, No. 7, 1985, pp. 1129-1130.
23. Childs, R. E., Nixon, D., Keefe, L. R., and Rodman, L. C., "A Study of Compressible Turbulence," AIAA-93-0659.
24. Launder, B. E. and Rodi, W., "The Turbulent Wall Jet - Measurement and Modeling," Ann. Review of Fluid Mech., 1983, pp. 429-459.
25. Witze, P. O. and Dwyer, H. A., "The Turbulent Radial Jet," J. Fluid Mech., Vol. 75, Part 3, 1976, pp. 401-417.
26. Sohn, C. H., Choi, D. H., and Chung, M. K., "Calculation of Plane-of-Symmetry Boundary Layers with a Modified $k-\epsilon$ Model," AIAA J., Vol. 29, No. 3, 1991, pp. 395-400.
27. Childs, R. E. and Caruso, S. C., "Assessment of Modeling and Discretization Accuracy for High Speed Afterbody Flows," J. Propulsion and Power, Vol. 7, No. 4, 1991, pp. 607-616.
28. Barata, J. M. M., Durão, D. F. G., and Heitor, M. V., "Turbulent Energy Budgets in Impinging Zones," Presented at the Eighth Symposium on Turbulent Shear Flows, Munich, 9-11 Sept. 1991.
29. Cimbala, J. M., Billet, M. L., Gaublonne, D. P., and Oefelein, J. C., "Experiments on the Unsteadiness Associated with a Ground Vortex," J. Aircraft, Vol. 28, No. 4, 1991, pp. 261-267.